Experimental Neurology 354 (2022) 114111

Contents lists available at ScienceDirect

Experimental Neurology

journal homepage: www.elsevier.com/locate/yexnr

Research paper

Virtual deep brain stimulation: Multiscale co-simulation of a spiking basal ganglia model and a whole-brain mean-field model with The Virtual Brain

Jil M. Meier [a,b,1,*], Dionysios Perdikis [a,b], André Blickensdörfer [a,b], Leon Stefanovski [a,b], Qin Liu [a,b], Oliver Maith [c], Helge Ü. Dinkelbach [c], Javier Baladron [c], Fred H. Hamker [c], Petra Ritter [a,b,1,*]

[a] Berlin Institute of Health at Charité – Universitätsmedizin Berlin, Berlin, Germany
[b] Charité – Universitätsmedizin Berlin, corporate member of Freie Universität Berlin and Humboldt-Universität zu Berlin, Department of Neurology with Experimental Neurology, Brain Simulation Section, Berlin, Germany
[c] Department of Computer Science, Chemnitz University of Technology, Chemnitz, Germany

ARTICLE INFO

Keywords:
Basal ganglia
Thalamus
The Virtual Brain
Multiscale co-simulation
Deep brain stimulation
Parkinson's disease
Spiking neuron models

ABSTRACT

Deep brain stimulation (DBS) has been successfully applied in various neurodegenerative diseases as an effective symptomatic treatment. However, its mechanisms of action within the brain network are still poorly understood. Many virtual DBS models analyze a subnetwork around the basal ganglia and its dynamics as a spiking network with their details validated by experimental data. However, connectomic evidence shows widespread effects of DBS affecting many different cortical and subcortical areas. From a clinical perspective, various effects of DBS besides the motoric impact have been demonstrated. The neuroinformatics platform The Virtual Brain (TVB) offers a modeling framework allowing us to virtually perform stimulation, including DBS, and forecast the outcome from a dynamic systems perspective prior to invasive surgery with DBS lead placement. For an accurate prediction of the effects of DBS, we implement a detailed spiking model of the basal ganglia, which we combine with TVB via our previously developed co-simulation environment. This multiscale co-simulation approach builds on the extensive previous literature of spiking models of the basal ganglia while simultaneously offering a whole-brain perspective on widespread effects of the stimulation going beyond the motor circuit. In the first demonstration of our model, we show that virtual DBS can move the firing rates of a Parkinson's disease patient's thalamus - basal ganglia network towards the healthy regime while, at the same time, altering the activity in distributed cortical regions with a pronounced effect in frontal regions. Thus, we provide proof of concept for virtual DBS in a co-simulation environment with TVB. The developed modeling approach has the potential to optimize DBS lead placement and configuration and forecast the success of DBS treatment for individual patients.

1. Introduction

Deep brain stimulation (DBS) is a neuromodulation technique that has shown beneficial effects for patients suffering from many different neurological disorders (Horn, 2019; Horn and Fox, 2020). DBS is an essential element in the therapeutic regime for movement disorders like Parkinson's disease (PD) (Deuschl et al., 2006; Vitek et al., 2020), dystonia (Kupsch et al., 2006) and essential tremor (Koller et al., 1997). It provides a treatment option for selected cases of medication-refractory epilepsy (Salanova et al., 2015) and obsessive-compulsive disorder (OCD) (Anderson and Ahmed, 2003; Franzini et al., 2010; Nuttin et al., 2008). For major depression (Mayberg et al., 2005), Tourette's syndrome (Ackermans et al., 2011), Huntington's disease (Gruber et al., 2014) and alcohol addiction (U. J. Müller et al., 2009), DBS has shown first treatment successes and is clinically applied on an experimental basis. Despite the benefits of DBS for many diseases, underlying mechanisms are so far poorly understood. At various scales of the brain, attempts have been made to model the outcome of DBS, from single-

* Corresponding authors at: Berlin Institute of Health at Charité – Universitätsmedizin Berlin, Berlin, Germany; Charité – Universitätsmedizin Berlin, corporate member of Freie Universität Berlin and Humboldt-Universität zu Berlin, Department of Neurology with Experimental Neurology, Brain Simulation Section, Berlin, Germany.
E-mail addresses: jil-mona.meier@bih-charite.de (J.M. Meier), petra.ritter@bih-charite.de (P. Ritter).
[1] postal address: Charité - Universitätsmedizin Berlin, Charité Campus Mitte (CCM), Brain Simulation Section, Robert-Koch-Platz 4, 10,115 Berlin, Germany

https://doi.org/10.1016/j.expneurol.2022.114111
Received 29 April 2021; Received in revised form 4 April 2022; Accepted 5 May 2022
Available online 13 May 2022

neuron to whole-brain models (Humphries et al., 2018). However, a multiscale model to bridge these different scales in a single DBS model has yet to be developed.

The most extensive research for DBS has been performed in movement disorders, which share pathology of the interactions between basal ganglia (BG), thalamus and cortex (Plotkin and Goldberg, 2019). The BG are anatomically defined by the striatum and the pallidum, which can be further separated in globus pallidus internus (GPi) and externus (GPe). Functionally, the regions of the subthalamic nucleus (STN) and the substantia nigra, whose degeneration is a key factor in the pathogenesis of PD (Damier et al., 1999; Fearnley and Lees, 1991), are often included in the BG because of their strong interactions with it (Albin et al., 1989). In the following, the term BG refers to "basal ganglia and related nuclei" (Lanciego et al., 2012) according to the widely used understanding as a functional unit of the extrapyramidal system (Heimer, 1983).

The hypothesis that PD patients often suffer from a decreased activity level in the thalamic region causing the motor function to be impaired, resulting in bradykinesia or akinesia, has a long history (DeLong, 1990; Humphries et al., 2018; Jahanshahi et al., 2015). This decreased activity in the thalamus is probably caused by pathological hyperactivity of the globus pallidus as a failure symptom of the dopaminergic system (Dostrovsky et al., 2002), a theory first formulated by the classical rate model of the BG (Albin et al., 1989). The clinically most relevant stimulation targets for PD are the GPi and STN (Horn and Fox, 2020). It is a common approach to model the neurons of these key regions for DBS as a network, employing mathematical descriptions of neuronal behavior and interactions (Yu et al., 2020). An extensive amount of previous literature exists modeling the connection from STN to GPe, the striatal microcircuit and different subparts of the cortico-basal-ganglia-thalamo-cortical loop as spiking networks (Yu et al., 2020). These subnetwork studies suggest that STN-DBS changes the efferences of the BG to the thalamus by suppressing the burst firing of the GPi (Guo et al., 2008; Rubin and Terman, 2004).

Most previously established models are based on a priori assumptions about dynamic changes in PD, i.e., assuming differences between PD and healthy subjects with regard to their functional connectivity strengths or their activity levels of striatal projection neurons (Humphries et al., 2018). Though these assumptions are well justified by empirical findings, they critically influence the model outcomes. In contrast, Hamker and colleagues proposed a data-driven spiking model of the BG (Baladron et al., 2019; Maith et al., 2021), that is a generic BG model has been fit to the individual subject data by optimizing its parameters such that features of the simulated activity correlated with the same features of the measurements. Recently, Maith et al. (2021) fitted this BG model for *20* PD patients after DBS implantation and *15* healthy controls with individual resting-state functional magnetic resonance imaging (fMRI) data. However, the whole cortex was so far modeled as a single spiking network node, lacking a whole-brain perspective.

The single-neuron and subnetwork models of the BG successfully suggest underlying mechanisms for the improvement of PD hypokinesia symptoms during DBS. However, they are not sufficient in describing the multitude of other effects that DBS potentially has on PD patients, e.g., rigidity, tremor and cognitive or behavioral changes (Irmen et al., 2019). Therefore, extending local DBS effects of the cortex-BG-thalamus loop towards a large-scale network should be the next goal in understanding DBS effects.

Previous studies explored mean-field approaches simulating the whole-brain perspective for virtual DBS (Saenger et al., 2017; van Hartevelt et al., 2014). Mean-field models make use of a physical simplification to enable simulating the average or so-called mean-field behavior of large populations. Simulating the whole brain with mean-field modeling has shown that DBS brought the patients' dynamical regime closer to a healthy one (Saenger et al., 2017; van Hartevelt et al., 2014). With respect to whole-brain mean-field simulations, The Virtual Brain (TVB, *thevirtualbrain.org*) (Ritter et al., 2013; Sanz Leon et al., 2013) offers a neuroinformatics platform to simulate the effects of a virtual DBS. This in silico computation of the whole-brain effects of DBS requires only the MRI data of an individual patient as an input. Simulated brain activity with TVB reproduces empirical phenomena accurately over different modalities (Schirner et al., 2018). Applying TVB in combination with simulated stimulation has shown resemblance with functional resting-state networks (Spiegler et al., 2016, 2020) and with electroencephalography (EEG) patterns after transcranial direct current stimulation (Kunze et al., 2016). However, virtual DBS has not yet been investigated with TVB.

The different computational studies demonstrating the effects of PD and/or DBS on the BG network, from single-neuron studies to whole-brain networks, exemplify the multiscale nature of this research field (Humphries et al., 2018). So far, the whole-brain DBS modeling literature stands isolated from the extensive literature on spiking neural networks of the BG. Only region-wise properties have been compared. None of the dynamical insights from the spiking network literature have been incorporated into the mean-field modeling approaches of DBS. Therefore, in this study, we aim to demonstrate the framework for a multiscale co-simulation approach of virtual DBS. Our goal is to bridge the microscale of single neurons towards the recorded whole-brain signals in one simulation framework, which permits a holistic and comprehensive integration of existing findings. To run whole-brain mean-field simulations and additionally simulate any region's fine-scale neuronal dynamics, including spikes generated by inhibitory and excitatory neurons inside the region, we can use the recently developed TVB-multiscale co-simulation toolbox (Schirner et al., 2022). TVB-multiscale extends TVB to perform multiscale co-simulations, whereby most of the nodes are simulated with TVB as mean-field models, and a few selected nodes are modeled as spiking networks by another suitable simulator.

In this study, we combine the detailed spiking network model by Maith et al. (2021) for the BG with mean-field simulations in TVB for all cortical regions. We interface the spiking network software ANNarchy with TVB to build the TVB-ANNarchy co-simulation framework (Schirner et al., 2022). As an underlying connection between BG and cortical regions, we utilize a recently published normative connectivity atlas of these tracts (Petersen et al., 2019) and combine it with individually - that is subject-specific - fitted probabilities and weights from Maith et al. (2021) for the connections among the BG regions. As a first proof of concept, we simulate resting-state conditions for an exemplary control and PD patient network and perform virtual DBS targeting STN and GPi in the patient network. Next, we validate our model by comparing the effects of virtual DBS against results from literature. Our study addresses the following limitations of previous whole-brain DBS modeling studies:

1) We incorporate a previously validated spiking network model of the subnetwork of the BG within our whole-brain modeling.
2) We use an underlying (normative) connectome, which includes the STN, and combine it with individually fitted connectivity data to create an individual patient and control multiscale network.

In this way, we offer a computational model that holds the potential to be easily translated towards the individual patient level and used as a 'sandbox' model before future DBS surgeries.

2. Materials and methods

2.1. Spiking network model for the basal ganglia

The spiking network model and its dynamics (including parameters) were taken from a previous publication (Maith et al., 2021) (Fig. 1). Eight neuronal populations were included, each with different properties. The cortex consisted of 600 excitatory neurons coupled with 150 inhibitory neurons (possessing a self-inhibitory connection). From the excitatory population of the cortex, spikes were transmitted to the STN,

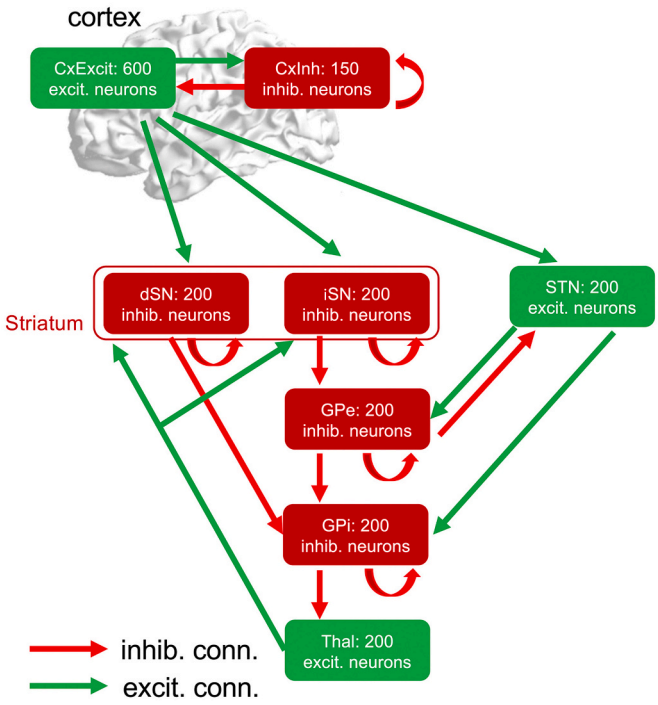

Fig. 1. Structure of the basal ganglia spiking model. Previously published detailed basal ganglia (BG) model by (Maith et al., 2021). We implemented this model inside our TVB-ANNarchy framework with the underlying previously optimized connection weights and probabilities for the data of one control and one PD patient (taken from (Maith et al., 2021)). The direct pathway is shown here as the path from the excitatory cortical neurons over the direct striatal projection neurons to the GPi. Similarly, the indirect pathway goes from the cortex, over the indirect spinal projection neurons and the GPe towards the GPi. The third pathway through the BG is the cortex-STN-GPi pathway, which is also called the hyperdirect pathway. CxExcit: excitatory population of the cortex; CxInh: inhibitory population of the cortex; GPi: internal globus pallidus; GPe: external globus pallidus; STN: subthalamic nucleus; dSN: striatum, direct striatal spiny projection neurons; iSN: striatum, indirect striatal spiny projection neurons; Thal: thalamus; excit.: excitatory; inhib.: inhibitory; conn.: connection.

as well as the striatum. The striatum was modeled with two different inhibitory neuronal populations, the direct (dSN) and the indirect (iSN) striatal spiny projection neurons, each with a self-inhibitory connection. The GPe and GPi were each represented by inhibitory neurons with a self-inhibitory connection. The thalamus was also modeled as a spiking network node.

Each spiking network population was modeled by an enhanced version of the Izhikevich model (Izhikevich, 2004). For details of this previously published model, we refer to the Supplementary Material. Maith et al. (2021) optimized the connection probabilities and weights between the nodes to fit empirical fMRI blood-oxygen-level-dependent (BOLD) signal correlation data for each individual and each hemisphere separately. We used this optimized data from one of the controls and one of the patients (left hemisphere only). We selected these subjects as representatives of their groups because their regional firing rates were close to the respective mean values. This computational model was implemented with the software Artificial Neural Network architect (ANNarchy), used for spike and rate coding of neuronal populations, as well as a combination of both in a single network (Vitay et al., 2015). Network models in ANNarchy are defined through equations written in "natural language". ANNarchy has been used to implement models of the BG pathways (Baladron et al., 2019; Baladron and Hamker, 2020; Gönner et al., 2020; Villagrasa et al., 2018), spatial attention and vision (Bergelt and Hamker, 2019; Jamalian et al., 2017; Larisch et al., 2021) and learning and memory (Gönner et al., 2017; J. Müller et al., 2018; Schmid et al., 2019).

2.2. Multiscale co-simulation of TVB and ANNarchy

Every node in the TVB network represents a brain region and its dynamics are simulated with a mean-field approximation. The nodes are connected with weights and delays (computed from tract lengths given a transmission speed) that can be determined for individual subjects employing DTI. As a mean-field model for the cortical regions, we chose the reduced Wong-Wang-model (Deco et al., 2013), which is often used to replicate fMRI data (Aerts et al., 2018; Klein et al., 2021; Schirner et al., 2018) and based on the Wong-Wang model (Wong and Wang, 2006) (details in the Supplementary Material). We used the version of this model that represents each TVB region as one excitatory population. Given the fact that the inhibitory population in the Maith et al. (2021) network neither projects to other regions nor receives any such projections, the inhibitory population could be omitted from explicit modeling, without affecting otherwise our network dynamics. For an overview of all variables used in this study, we refer to Supplementary Table 1. In the TVB-multiscale framework (Schirner et al., 2022), co-simulation is based on the concept of TVB "proxy" nodes that are created inside the spiking network (Fig. 2). TVB "proxy" nodes are either stimulating devices, thereby mimicking TVB cortex node dynamics (i.e., mean-field spiking rates) and coupling to the spiking nodes, or output (e.g., recording) devices, thereby extracting spiking dynamics to be transmitted to TVB. Thus, TVB and the spiking network simulator communicate on the level of neuronal populations' mean-field activities. TVB-multiscale, which is continuously expanding, is freely available on github (github.com/the-virtual-brain/tvb-multiscale) and interfaces TVB with different spiking network simulators (currently Neural Simulation Technology (NEST) (Eppler et al., 2008) and ANNarchy).

Since the previous BG model implementation was fitted with empirical data using ANNarchy (Maith et al., 2021), we built an interface between ANNarchy and TVB. We developed python code to incorporate the ANNarchy simulator into TVB-multiscale (details in the Supplementary Material). We validated our implementation of the spiking network by Maith et al. (2021) against the authors' original ANNarchy code by performing short simulations without noise for the two selected subjects (Supplementary Table 3).

Each TVB cortex mean-field node n' (prime notation for nodes modeled only as mean-fields nodes in TVB) couples to a node n modeled in ANNarchy (notation without prime for the spiking regions) via the instantaneous spike rate variable $R_{n'}(t)$, which drives a population of $N_{neurons} = 600$ neurons (same size as for the excitatory cortex node of the spiking network by Maith et al. (2021)) generating correlated spike trains

$$w_{n'n}\left\{\delta\left(t-\left(\tau_{n'n}+t_{jk}\right)\right)\right\}_{j\in\{1,\ldots,N_{neurons}\}}^{t_{jk}\in[t,t+dt]}$$

where t_{jk} stands for the spike time t_k of the neuron with index j in the population of the "proxy" node n' and δ is the Kronecker delta. The generated spikes were weighted by $w_{n'n}$ and delayed by $\tau_{n'n}$ based on the TVB connectome and the optimized weights for each subject (see below). For details of the spike trains' generation, we refer to the Supplementary Material.

In the other direction, each node n modeled in ANNarchy updates the state of the corresponding TVB mean-field node n since it is still represented in the TVB model and couples to TVB nodesn'. The update utilizes an ANNarchy monitor that records spikes for each TVB time step. The recorded spikes are converted to an instantaneous population mean rate that overwrites an auxiliary TVB state variable, called the input rate $R_{inn}(t)$. The latter drives a linear integration equation of another auxiliary TVB state variable, named integrated rate $R_{intn}(t)$, which, in its turn, acts as a smoothing low pass filter

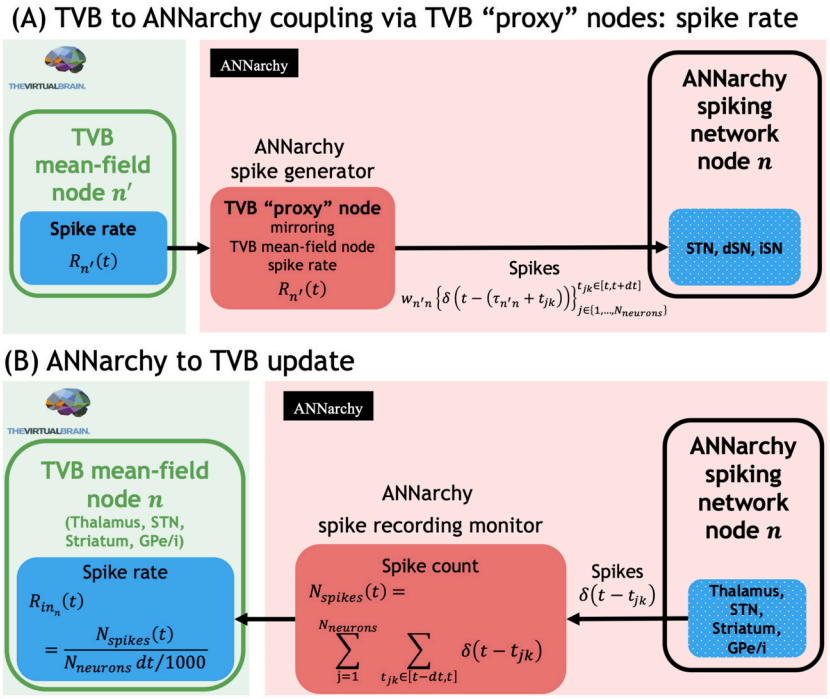

Fig. 2. Implementation of the interface for the multiscale model. (A) TVB to ANNarchy coupling is channeled via TVB "proxy" nodes in the ANNarchy network, implemented as neuronal populations generating correlated spike trains. Thus, the instantaneous mean-field spike rate is transformed into individual neurons' spike trains for the respective time interval. (B) ANNarchy to TVB state update via the ANNarchy monitors, which record the spikes for each time interval $[t-dt, t]$ to compute the population's spike rate. This spike rate then overwrites the respective TVB state variable.

$$\dot{R}_{int_n} = -\frac{1}{\tau_{int}}\left(R_{int_n}(t) - R_{in_n}(t)\right)$$

to have time series similar to the TVB mean-field ones, where $\tau_{int} = 100ms$ is the time constant of the integration and

$$R_{in_n}(t) = \frac{\sum_{j=1}^{N_{neurons}} \sum_{t_{jk}\in[t-dt,t]} \delta(t-t_{jk})}{N_{neurons} \cdot dt/1000}$$

provides the number of spikes per second. Finally, the integrated rate $R_{intn}(t)$ overwrites the state variable $R_n(t)$ of the TVB model. All the rest of the TVB mean-field nodes n' follow the equations of the mean-field model described in the Supplementary Material. We simulated two ANNarchy time steps (of $0.05ms$) for every TVB time step ($dt = 0.1ms$).

2.3. Underlying connectivity

To connect the TVB nodes and the spiking network simulator, we needed to assign connectivity weights for the paths between the BG regions and the cortex. Acquiring accurate data for those tracts is challenging because structural MRI data inherits many limitations (Jones et al., 2013; Thomas et al., 2014). Recently, Petersen et al. (2019) published a state-of-the-art axonal pathway atlas for the human brain that combines previous results from histological and imaging data literature with expert knowledge of neuroanatomists and brain-imaging scientists who collaborated on defining those tracts applying a holographic visualization technique (Petersen et al., 2019) (details to be found in the Supplementary Material). We used this normative tract data by Petersen et al. (2019) to include a fine-grained parcellation for the BG and the thalamus (based on CIT-168 brain atlas (Pauli et al., 2018)) and detailed data of their pathways to and from the cortical regions because of its current use for clinical DBS planning (Noecker et al., 2021). Whereas Maith et al. (2021) used the motoric parts of the BG regions only in their parcellation, we used the complete BG regions as a first approach. This difference implies that the connectivity of Maith et al. (2021) was more limited than ours regarding the outside connections of the BG to the cortex. For the cortex, the automated anatomical labeling (AAL) atlas parcellation was applied (Rolls et al., 2015; Tzourio-Mazoyer et al., 2002). The tract data files of Petersen et al. (2019) were extracted from Lead-DBS software (www.lead-dbs.org; (Horn and Kühn, 2015)) in the DBS Intrinsic Template Atlas (DISTAL) space (Oxenford et al., 2021) and the number of streamlines between each region pair was counted. This procedure resulted in a whole-brain matrix for the pathways between the cortex and the BG structures.

Some additional preparation steps have been performed on the connectome. As a first demonstration and because Maith et al. (2021) also treated the hemispheres in isolation, we focused on the left hemisphere only. Thus, all regions belonging to the right hemisphere and the vermis have been deleted from the connectome together with all their connections. Additionally, the connections from the inhibitory neuronal populations in the BG (GPe, GPi and striatum) to any cortical regions have been set to zero as it is currently not much known about how these projections contribute to movement regulation (Abecassis et al., 2020; Chen et al., 2015; Cui et al., 2021; Saunders et al., 2015), leaving in this direction only the connections from the thalamus and the STN to the cortex. In the other direction, we only allowed cortical input projections towards the STN and the striatum into the spiking network similar to the Maith et al. (2021) network. Forcing such a prior on the model is necessary for keeping the spiking dynamics as close as possible to the previously optimized network by Maith et al. (2021). The resulting connectome included 57 regions (for a list of all included regions: Supplementary Table 4). Its weights were normalized first by the maximum sum of all the incoming connection weights over all regions and then again by the 99th percentile of all weights to scale all connection weights in a smaller range. After these steps to generate the connectome, we obtained the connectivity weights among all 57 regions (Supplementary Figs. 5–6). We discovered that 30 regions were disconnected from the rest, meaning that these regions had no tracts based on the Petersen et al. (2019) data. We call these regions isolated or disconnected regions. The reason for that lies in the used normative atlas of Petersen et al. (2019), which focuses on the connections between the cortex and the basal ganglia and does not include cortico-cortical connectivity. The resulting connected regions in the connectome are the motor regions, the frontal lobe and orbital and cingulate gyri as well as the insula. Only the activity of the connected regions influences the rest of the network and therefore our simulation results.

The previous work of Maith et al. (2021) optimized the connection

probabilities and weights among BG regions per individual to best fit the empirical fMRI data. To personalize the normative connectome, we replaced the network among the BG and thalamus regions with the optimized weights computed by Maith et al. (2021) for the control subject and the PD patient, respectively (Fig. 3). This 'hybrid' connectome constituted normative connectome weights among the cortex regions and between cortex and BG (which will also be multiplied with the interface factors, see next section) but included individually fitted connection weights and probabilities for the spiking network of the BG. The connectome used for the patient and the control simulations differed only in the BG spiking network connections. We visualized the BG spiking network connection weights from the PD patient and the control in the upper row of Fig. 3. The biggest differences in connectivity weights between the patient and the control were in the inhibitory

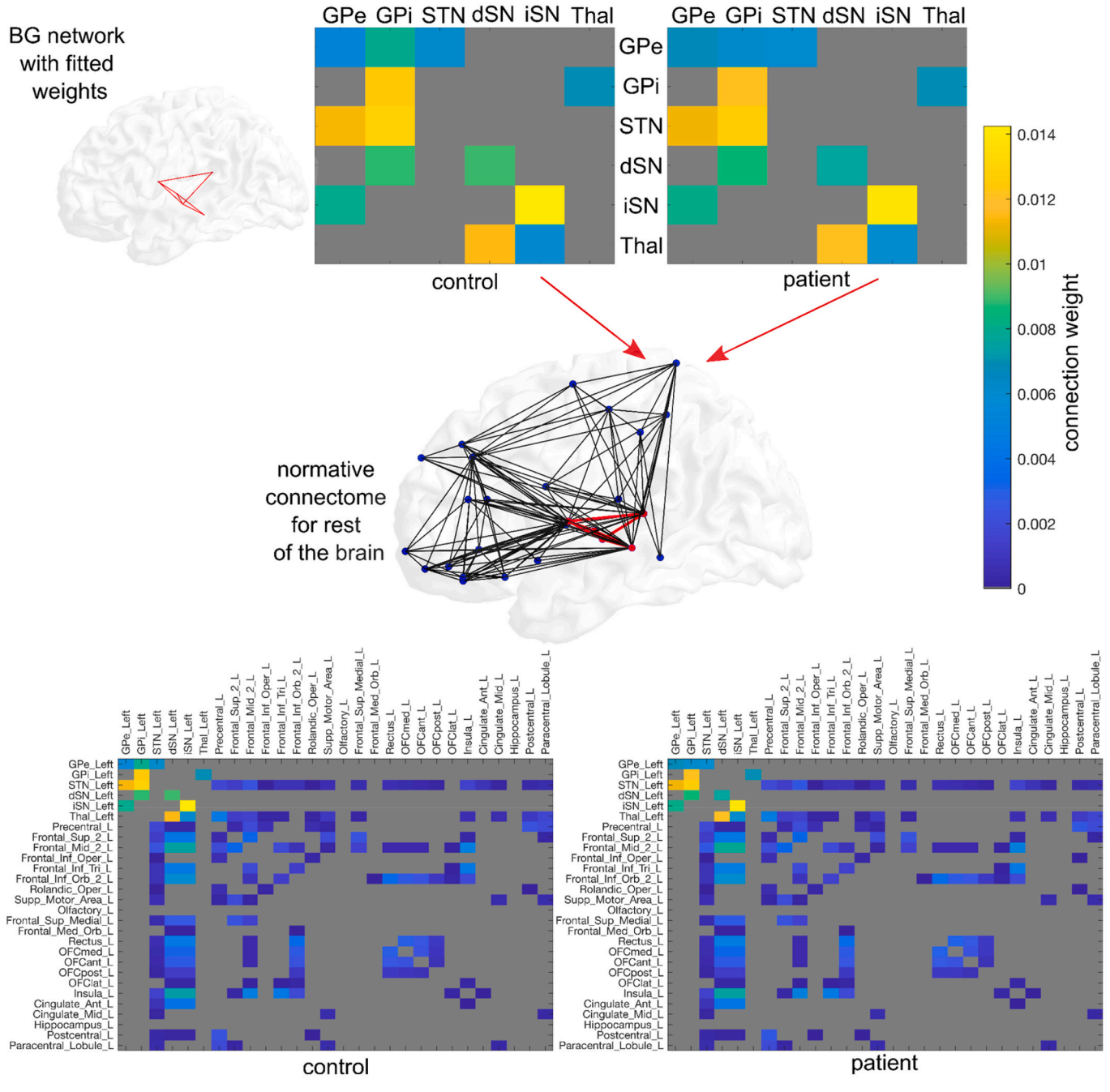

Fig. 3. Underlying connectome. The optimally fitted connectivity data from Maith et al. (2021) for the left hemisphere of the analyzed control and patient (upper panels) overrode the within-BG connection weights inside the connectome (upper left corner of the larger matrices) based on (Petersen et al., 2019). Note that the connectivity in the BG network is unidirectional whereas the connectivity among the cortical regions is bidirectional. Each entry in any of the matrices represents the normalized number of streamlines that start in the region marked on the horizontal axis and end in the region marked on the vertical axis. The brain network in the middle shows all connections taken from the individually fitted weights and the BG regions in red and the other regions in blue with the connections taken from the normative connectome of the atlas by Petersen et al. (2019) represented in black. The lower two matrices represent the matrices used for the control (left) and the patient (right) simulations, respectively. For visualization purposes, all isolated nodes have been disregarded and the normalized Petersen et al. (2019) connections have been brought to the same range as the optimally fitted connectivity weights from Maith et al. (2021). GPi: internal globus pallidus; GPe: external globus pallidus; STN: subthalamic nucleus; Thal: thalamus; dSN: striatum, direct striatal spiny projection neurons; iSN: striatum, indirect striatal spiny projection neurons. (For interpretation of the references to color in this figure legend, the reader is referred to the web version of this article.)

connection weight from GPe to itself and to GPi. In the patient parameters, this connection weight from GPe to GPi was only 78% of the weight in the control parameters, meaning that the patient had a lower connection weight from GPe to GPi than the control. The self-inhibition weight of GPe was much higher in the patient than in the control, i.e. 125% of the control's connection weight, whereas the self-inhibition connection weight of the dSN was smaller in the patient than in the control (85% of the control's weight). In the other connection weights, the patient value was between 97% and 105% of the control value. If we also consider the fitted connection probabilities from Maith et al. (2021), then we find differences between the patient and control in all connections inside the spiking network, except for the excitatory connections from the STN towards the pallidum, from the thalamus towards the iSN and the self-inhibition of the GPi. However, the focus of the current work were not these cross-sectional connectivity differences but rather how the different control and patient networks that were previously fitted affect the rest of the cortical regions and how DBS counteracts this difference. For detailed comparisons between patients' and controls' connectivity, we refer to Maith et al. (2021). For the presentation and for determining the couplings between the two scales, we adjusted the normative weights to be in the same range of values as the optimized connection weights by scaling them with the ratio C_{norm} between the 95th percentiles of both weight distributions. The global coupling G of the TVB mean-field model was set for each subject to $G = 15/C_{norm}$, i.e., we are canceling the above normalization for the weights among the TVB nodes (see next section for the exact procedure of selecting the value of 15). The conduction speed was set to $4m/s$, thus, determining the time delay of couplings among all nodes of the multiscale model. The tract lengths among all regions were approximated by the Euclidean distance between their center coordinates (Supplementary Fig. 2).

2.4. Fitting the co-simulation model to individual dynamics

We implemented the previous BG model by Maith et al. (2021) inside our TVB-ANNarchy framework (Fig. 4). For the multiscale model ("TVB-cortex model"), we replaced the spiking node "cortex" with the whole brain connectomic model in TVB (Fig. 5). However, the input from the multitude of the TVB mean-field nodes leads to different driving dynamics of the spiking network than in Maith et al. (2021). The previous BG model represented the cortex by an excitatory and an inhibitory population, whereas the chosen version of the reduced Wong-Wang mean-field model represents each cortical region only as an excitatory population. We aimed for TVB driving dynamics that would exhibit (a) a mean firing rate across all TVB nodes of $10 - 15$ Hz similar to motor cortex neurons at rest (Velliste et al., 2014), where the variation over TVB regions in rate values is determined by the structural connectome; (b) low amplitude random fluctuations of the rate around the equilibrium point of the above mean rate, resembling the rate dynamics of the cortex node in Maith et al. (2021) (c) a correlation of 0.3 among the neurons' spiking to resemble Maith et al. (2021), which in Maith et al. (2021) is due to the internal connectivity of the spiking cortex node populations (more details in the Supplementary Material). We set the operation point of the TVB mean-field network by progressively increasing global coupling G until an equilibrium point was reached with a mean firing rate across the whole TVB brain approaching 15 Hz (for $G = 15/C_{norm}$) from below via a few "trial and error" simulations. Further precision in the final G value would not change our results since

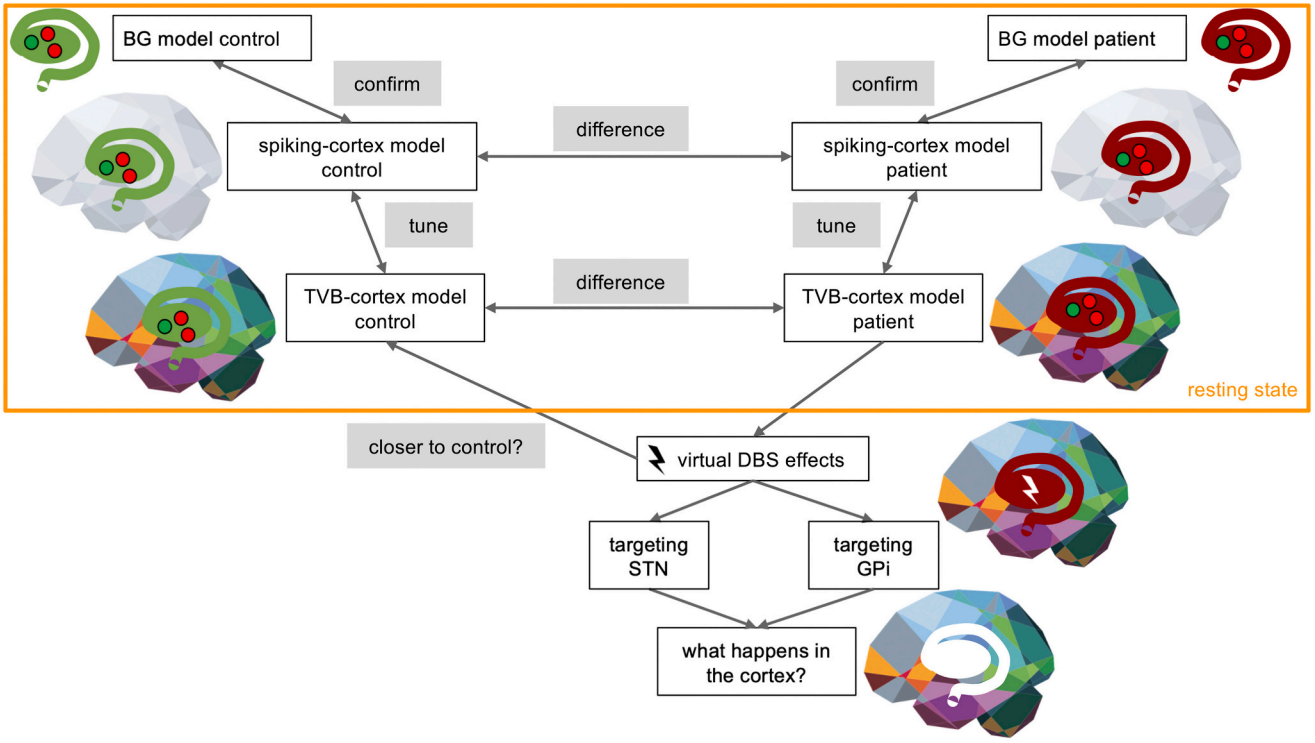

Fig. 4. Schematic overview of our study design. The basal ganglia (BG) model of one control and one Parkinson's disease patient were taken from the previous study (Maith et al., 2021). Next, we implemented the previous model inside our TVB-ANNarchy framework, not yet activating TVB, the so-called "spiking-cortex model". We confirmed that this implementation reaches similar firing rates as the one from the previous study (step "confirm"). As a second step, we replaced the spiking-cortex node with mean-field simulations using TVB to obtain the so-called "TVB-cortex model. To stay in the range of the previously confirmed firing rates for the BG regions, we fine-tuned the connection weights from TVB to ANNarchy for the TVB-cortex models of the control and the patient. So far, all of the described modeling steps were taken in resting-state conditions. As a third step, we stimulated the STN and the GPi as two frequently targeted regions virtually (virtual DBS) and analyzed the effects for the BG spiking network as well as for the cortical regions. We analyzed whether virtual DBS could bring the patient's brain dynamics closer to the healthy one. Whenever there is a brain next to the model (even when it is grayed out), the simulation took place inside the TVB-ANNarchy environment.

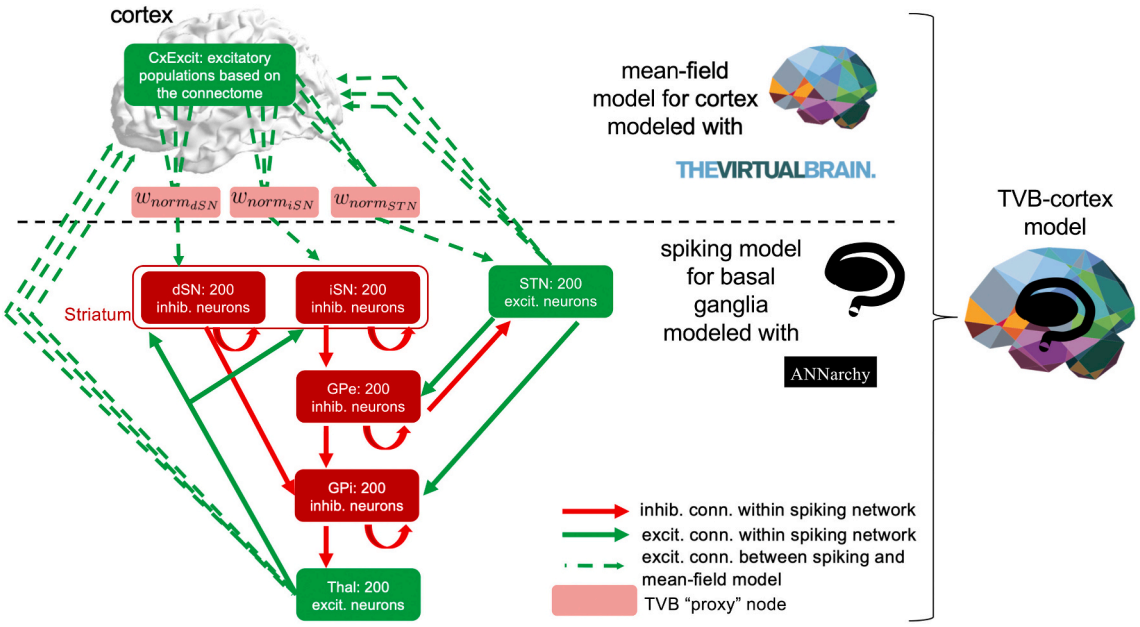

Fig. 5. Structure of the co-simulation model. The cortex node was replaced by a whole-brain network simulated with The Virtual Brain. The interactions among the cortical regions were simulated with a mean-field model and The Virtual Brain (TVB). The computational spiking model was simulated with ANNarchy. Together, these two models form the multiscale model, the so-called TVB-cortex model. Interactions between the mean-field and the spiking model were defined by the connection weights of the underlying connectome between all involved region pairs. Connections from cortical regions towards the spiking network (i.e., in our case towards dSN, iSN and STN) were bundled together for each of the regions receiving input from the cortex. In addition, the bundled connections were weighted with the interface weights w_{normn}, $n \in \{dSN, iSN, STN\}$ to regulate the incoming driving activity of the network. CxExcit: excitatory populations of the cortex; GPi: internal globus pallidus; GPe: external globus pallidus; STN: subthalamic nucleus; dSN: striatum, direct striatal spiny projection neurons; iSN: striatum, indirect striatal spiny projection neurons; Thal: thalamus; excit.: excitatory; inhib.: inhibitory; conn.: connection.

any small difference in that value would be counteracted by corresponding small differences in the scaling of the coupling from the TVB cortex to the spiking basal ganglia network (see below). After the equilibrium point was approximated, we increased the additive white noise to a standard deviation of 10^{-4} allowing small fluctuations around the equilibrium point without changing the pattern of nodes with higher firing rates (Supplementary Fig. 3 displays a characteristic TVB time series during co-simulation).

For the multiscale TVB-cortex model, the three connections from cortex to STN, dSN and iSN were substituted by the respective set of connections from each of the corresponding TVB nodes (Fig. 5). For scaling these connections, we created a "spiking-cortex model" by substituting the cortex node of the network from Maith et al. (2021) with an ANNarchy spike generator identical to the one used as TVB "proxy" nodes (Supplementary Material). The spiking-cortex model acted as the "bridge" between the noisy TVB cortex driving the multiscale model and the Izhikevich population spiking cortex of Maith et al. (2021). With this model, we performed resting-state simulations for both subjects. Then, we tuned - again via a few "trial and error" co-simulations - three interface factors w_{normn}, $n \in \{iSN, dSN, STN\}$, scaling all TVB connections to STN, dSN and iSN, respectively, to approximate the mean population rates of the spiking-cortex model (Fig. 5, Supplementary Table 1). These interface factors multiply the TVB connectome weights $C_{n'n}$ resulting in the interface weights $w_{n'n} = w_{normn} \cdot C_{n'n}$ (Fig. 2A). This step was also taken to ensure that dSN and iSN can receive different input while the striatum connectivity is equally strong for them. This way, the sum across all TVB nodes n' is the resulting total weight of the cortex input to the BG spiking populations, which then has an effect close to the one of the optimized weights in Maith et al. (2021). The differences between the patient and the control in the interface factors were very small (Supplementary Table 1, maximally 0.022 difference in the factor value). The final mean firing rates were within 1 *Hz* for all spiking populations except for the thalamus of the control network, which was within 2 *Hz* (Supplementary Table 5, Supplementary Fig. 4). The spiking-cortex model is only an intermediate development step for validation purposes and the TVB-cortex model is the final model.

For the results of the TVB-cortex simulations, we simulated each condition *10* times, randomly selecting initial conditions for the TVB state from a normal distribution with mean equal to the initial conditions used originally for fitting the resting-state simulations and standard deviation *0.1* (Supplementary Material). The simulation length for all of our simulations was 1500*ms*. After each simulation, we computed the mean firing rate over the last 1000*ms*.

2.5. Implementation of the DBS stimulus

Besides the resting-state co-simulations, we applied a stimulus to our multiscale model (starting at 400*ms* and lasting till the end) inside either GPi or STN as possible target regions (Fig. 5). We simulated the propagation of these stimuli and the whole-brain response to them to provide a first proof of concept of the possibilities of this kind of multiscale modeling. We tested the virtual DBS stimuli within the spiking-cortex model and the TVB-cortex model.

To the GPi, we applied a continuous constant inhibitory current stimulus of an amplitude of $-10pA$ aiming at reducing its firing rate and therefore disinhibiting the thalamus. This simple continuous inhibitory stimulus was chosen for the GPi since the effect of GPi-DBS on the firing rate of the GPi is well known to be inhibitory and we thus opted to directly implement this inhibitory effect. For the other DBS simulations, we applied two realistic stimuli to STN, a monophasic and biphasic pulse-like current because the former is the most commonly implemented stimulus in previous DBS simulation studies (Yu et al., 2020) and the latter is used in clinical practice (Krauss et al., 2021) (Fig. 6). The monophasic stimulus is adapted from (Michmizos and Nikita, 2011) and the biphasic stimulus is similar to the one used in (Liu et al., 2020) (details in the Supplementary Material). We chose stimulus frequencies of 120 Hz for the monophasic and 130 Hz for the biphasic stimulus to be close to the ones used in clinical practice (Supplementary Table 1).

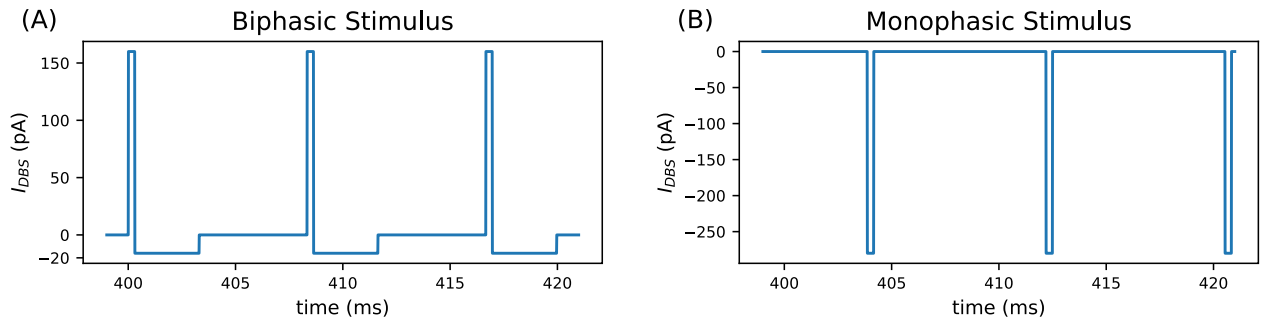

Fig. 6. STN-DBS stimulus patterns. The first three cycles of the (A) biphasic and (B) monophasic stimuli applied for the virtual DBS targeting the STN region.

2.6. *Effects of the stimuli on cortical regions*

To investigate the effects of the different stimuli on the cortex, we compared our resting-state TVB-cortex simulations with the simulations including the stimuli for the patient network. We also investigated cortical differences between the resting-state condition of the control and the patient. For these comparisons, we calculated the region-wise difference of cortical firing rates between simulations. Firing rates were averaged over the last 1000*ms* of a simulation. In the resting-state case of comparing the patient and the control, we subtracted the average firing rates of the control's resting-state simulation from the ones obtained with the patient network, following this formula for the normalized difference in average firing rate D_n^{rs} between the patient and the control for any region n

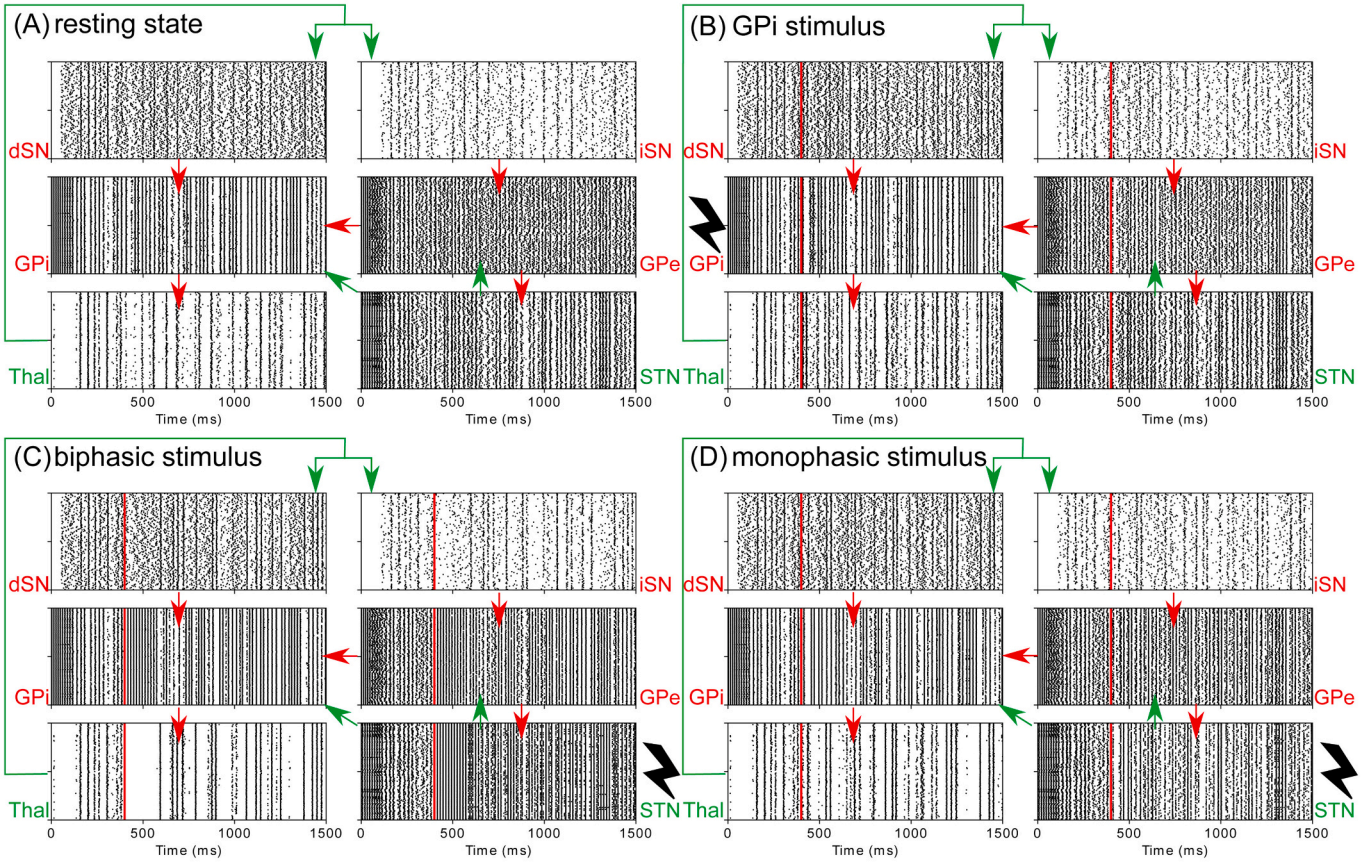

Fig. 7. Resting-state and DBS simulation results of the full co-simulation model implemented in TVB-ANNarchy for the patient network. The cortex is represented by the full-scale TVB model with a neural-mass model for each region, i.e., the TVB-cortex model results are displayed. The raster plots of the regions simulated with ANNarchy are shown here. On the y axis, the 200 neurons are listed in the respective region. Each dot in the raster plot represents a spike time of an individual neuron. Vertical black bars in the raster plot, thus, represent synchronous firing activity of all neurons. Mean firing rates are calculated based on the last 1000 ms of each simulation. (A) Results of the resting-state simulation for the patient's network. (B) Results of a virtual DBS simulation targeting the GPi with an inhibitory continuous constant current stimulus for the entire remaining duration of the simulation. The disinhibiting effect of the GPi stimulation (from 400 ms onwards) towards the thalamic activity can be observed in the visualized raster plots. (C) Results of a virtual DBS simulation targeting the STN with a biphasic stimulus. (D) Results of a virtual DBS simulation targeting the STN with a monophasic stimulus. The red vertical lines in the plots represent the start of the respective stimulus. Red (green) arrows visualize inhibitory (excitatory) connections among the regions. Region names written in red (green) color-code an inhibitory (excitatory) population. GPi: internal globus pallidus; GPe: external globus pallidus; STN: subthalamic nucleus; dSN: striatum, direct striatal spiny projection neurons; iSN: striatum, indirect striatal spiny projection neurons; Thal: thalamus. (For interpretation of the references to color in this figure legend, the reader is referred to the web version of this article.)

$$D_n^{rs} = \frac{\overline{R}_{n_{rs}}^{patient} - \overline{R}_{n_{rs}}^{control}}{\frac{1}{N}\sum_{m=1,\ldots,N}\left|\overline{R}_{m_{rs}}^{patient} - \overline{R}_{m_{rs}}^{control}\right|}$$

where $N = 57$ is the total number of regions, $\overline{R}_{n_{rs}}^{patient}$ and $\overline{R}_{n_{rs}}^{control}$ are the average firing rate of region n for the resting-state simulation of the patient and control, respectively. For evaluating the cortical effects of the different stimuli, we subtracted the resting-state average firing rates $\overline{R}_{n_{rs}}^{patient}$ from the ones of the stimulus-induced time series $\overline{R}_{n_{stim}}^{patient}$. The following equation D_n^{stim} describes the normalized difference in average firing rate between resting and stimulated states for the patient. In addition, the resulting regional differences were normalized by the mean over the absolute value of the obtained regional differences, for each subtraction separately (denominators in the above equations).

$$D_n^{stim} = \frac{\overline{R}_{n_{stim}}^{patient} - \overline{R}_{n_{rs}}^{patient}}{\frac{1}{N}\sum_{m=1,\ldots,N}\left|\overline{R}_{m_{stim}}^{patient} - \overline{R}_{m_{rs}}^{patient}\right|}$$

All of our code is publicly available (https://github.com/the-virtual-brain/tvb-multiscale/tree/Meier_etal_ExpNeur2021).

3. Results

For the multiscale TVB-cortex model, we visualized the raster plots of the spiking-network regions for the four conditions, resting-state, GPi-DBS, STN-DBS with a monophasic and STN-DBS with a biphasic stimulus (Fig. 7). Comparing the resting-state firing rates, the largest difference between the patient and the control can be found in the thalamus (Fig. 8 and Supplementary Table 4). The stimuli applied in the patient network caused the biggest changes in firing rate in the stimulated regions themselves (STN or GPi, respectively) and also in the thalamus (Fig. 8 and Supplementary Table 4). The GPi-DBS simulation induced disinhibition of the thalamus from the GPi, allowing the thalamus to fire more than in the resting-state condition. Both STN-DBS simulations, however, also showed increased thalamic activity compared to the resting state but together with an increased firing in the GPi (Fig. 8). Compared with the resting-state firing of the control, the patient seems to come closer to the rates of the control in multiple regions of the BG during all DBS scenarios (Fig. 8). The common mechanism over all three stimulation protocols was the increase in thalamic activity. Thus, the thalamus firing rate seems to "normalize" towards the healthy regime during virtual DBS.

Comparing the resting-state activities of the cortical regions between patient and control showed an increased average firing rate in the frontal regions and a decreased firing rate in the postcentral gyrus for the patient (Fig. 9A). Regarding the cortical effects of stimulation for the TVB-cortex model, we plotted the differences measured by the average

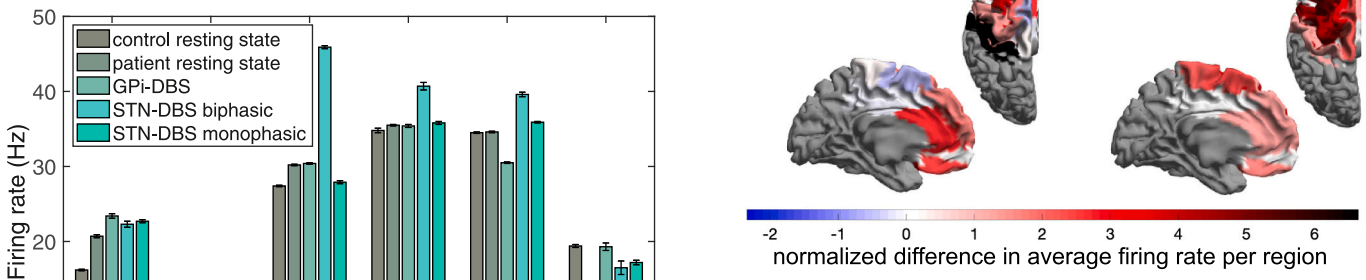

Fig. 8. Average firing rates obtained by different simulations of the TVB-cortex model. For each of the six spiking regions, the first and second bar represent the resting-state condition for the control and the patient, respectively. The latter three bars correspond to the three virtual DBS simulations in the patient network, i.e., GPi-DBS, STN-DBS applying a biphasic and a monophasic stimulus. The height of the bar represents the firing rate (in Hz) averaged over the last 1000 ms of the respective simulation and over the 10 simulation repetitions. The error bars have the length of twice the standard deviation over the average firing rates obtained over these 10 repetitions. For the thalamic firing rate, we observe a lower firing rate for the resting-state simulation of the patient compared to the control. During stimulation, the firing rate of the thalamus increased. GPi: internal globus pallidus; GPe: external globus pallidus; STN: subthalamic nucleus; dSN: striatum, direct striatal spiny projection neurons; iSN: striatum, indirect striatal spiny projection neurons; Thal: thalamus.

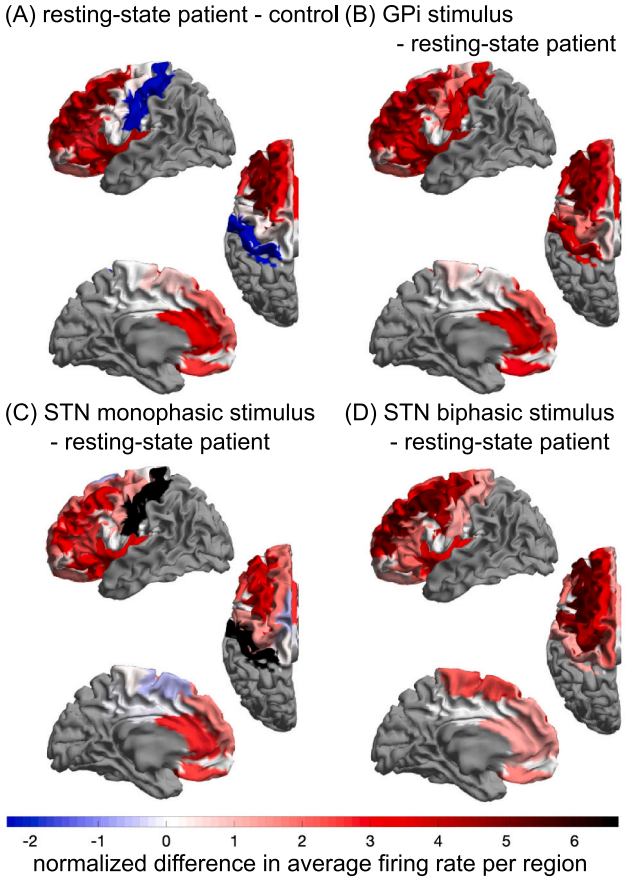

Fig. 9. Effects of the stimuli on cortical regions. We plotted the differences in averaged firing rate over the last 1000 ms of the simulation time on the template brain, subtracting the average rate obtained from one condition from the other. In addition, the resulting regional differences were normalized by the mean difference over the obtained regional differences for each subtraction separately. (A) The normalized difference in average firing rates is shown when subtracting the resting-state simulation results of the control from the ones of the patient. (B) The normalized difference in average firing rates is shown when subtracting the GPi stimulus simulation results from the resting-state simulation results of the patient. (C) The normalized difference in average firing rates is shown when subtracting the STN monophasic stimulus simulation results from the resting-state simulation results of the patient. (D) The normalized difference in average firing rates is shown when subtracting the STN biphasic stimulus simulation results from the resting-state simulation results of the patient. Thus, red (blue) colors indicate an increased (decreased) average firing rate of that specific region compared with the resting-state condition of the control (A) or the resting-state condition of the patient (B—D). Since our simulations are limited to the left hemisphere, we visualized the differences only for the left hemisphere. Gray regions represent disconnected regions. (For interpretation of the references to color in this figure legend, the reader is referred to the web version of this article.)

firing rate between the resting-state and each stimulus simulation per cortical region on the template brain in Fig. 9B-D. In all three virtual DBS simulations, the largest induced changes among the cortical regions were found in the frontal lobe and additionally in the postcentral gyrus for the monophasic STN stimulus. Altered levels of firing rates induced in the GPi and STN by the stimuli appear to be conveyed towards these cortical regions, altering their activity with respect to the resting state. Concerning the specific regions, the middle frontal gyrus and insula were for all three stimuli among the top five regions regarding the most increased firing rates induced by the stimulus. Interestingly, only the STN monophasic stimulus created a slight reduction of firing rate in the supplementary motor area (Fig. 9, bottom left, medial view). The differences in cortical activity are observed in motor, frontal, orbital and cingulate regions and in the insula because the other regions were disconnected in our connectome (Fig. 3, Supplementary Figs. 5–6).

4. Discussion

In this study, we introduced a multiscale modeling strategy for the brain network, which allows us to model the spiking network dynamics of the BG subnetwork in detail while simultaneously offering a whole-brain perspective of the evolving dynamics. We showed a first proof of concept that this new resulting TVB-multiscale model generates biologically plausible activity in resting state and during virtual DBS. This model has the potential to forecast DBS effects for different locations and different configurations on an individual patient level.

Our presented results show that the DBS stimulus introduced on our patient network causes disinhibition of the thalamus, leading to an increased firing rate during stimulation compared to resting state. Empirically, (Stefurak et al., 2003) and (Jech et al., 2001) found a BOLD signal increase in the thalamus by DBS. Additionally, (Horn et al., 2019) and (Mueller et al., 2018) showed an increase in coupling between the thalamus and the motor cortex by DBS using fMRI data. In (Saenger et al., 2017), the thalamus shows one of the largest changes in bifurcation parameters between DBS ON and OFF status based on fitted fMRI data. Electrophysiological studies in rats confirm the observed disinhibition of the thalamus during STN stimulation (Benazzouz et al., 1995, 2000). Even though our results are in line with the hypotheses formulated by the classical rate model (Albin et al., 1989), conflicting evidence from clinical studies suggests a broader perspective as reduced thalamic activity alone neither explains all symptoms of PD nor all existing therapeutic effects (Eisinger et al., 2019; Marsden and Obeso, 1994; Rodriguez-Oroz et al., 2009). As for the direct effect of the stimulus on the target region, the recent theory of short-term depression states that STN-DBS blocks the transfer of low-frequency oscillations downstream, e.g., towards GPe and GPi, and brings the thalamic activity back to healthy functioning (Humphries et al., 2018). Other theories exist about the effects of the DBS stimulus being of excitatory, inhibitory or disruptive nature on its neighboring areas and a consensus has yet to be reached in this research field (Chiken and Nambu, 2016). Still, our results show that the thalamic activity was brought back to healthy functioning by DBS, which is in line with the general mechanism of DBS (Humphries et al., 2018). Since the effect of the DBS stimulus on the STN is not yet completely clarified, we chose to test out two different stimuli, one increasing (biphasic) and one decreasing (monophasic) the firing rate of the STN. The difference in effects was probably largely caused by the maximum amplitude of the stimuli being positive (biphasic stimulus with strong excitatory current peak) or negative (monophasic stimulus contains only inhibitory current). The biphasic stimulus leads to a strong increase in firing activity in the STN, which is probably due to the depolarizing effect of the excitatory current leading to more spikes. A thorough grid-like exploration of different amplitudes would be out-of-scope for this first proof-of-concept study but will be included in future work using High Performance Clusters and parallel simulation design. Furthermore, the strong increase in STN firing rate during biphasic stimulation is in comparison only causing weak increases in the firing rates of the pallidum. This diminished transfer of the stimulus from the STN towards the pallidum can be explained by the high excitatory baseline current in GPi and GPe (which is necessary for the constant high firing rate, besides inhibition from striatum and lateral-inhibition). The added excitatory current in GPi and GPe due to the higher STN firing rate is probably relatively small compared to this baseline excitatory current.

The increased firing rates of the thalamus during our STN-DBS simulations are not caused by decreased GPi activity, which cannot be explained by the classical direct/indirect pathway model of BG. Empirical evidence supports the observed increased firing rates of GPi during STN stimulation (Reese et al., 2011), which were assumed to overwrite pathological activity patterns. One recent computational modeling study with optogenetic data of rodents has shown that increased GPi activity, when synchronized, is able to drive excitatory thalamic responses despite the inhibitory nature of the connection (Liu et al., unpublished results). The proposed underlying mechanism is that bursts of inhibition from GPi to thalamus can cause hyperpolarization and then post-inhibitory rebound firings of thalamus neurons. Post-inhibition spikes or bursts are characteristic behavior of the Izhikevich neuronal model used in this study (Izhikevich, 2004). Taking this unclear mechanism of pacing into account, our model provides computational evidence supporting a network effect leading to thalamic activation.

There have not been previous studies of multiscale co-simulation of DBS. PD is a multiscale disease (Kerr et al., 2013) with pathological mechanisms at many different scales, from deterioration observed in single neurons up to large-scale brain dynamics. Thus, in the attempt of modeling the broad perspective of potential treatment effects, one should also no longer focus on a single scale. One previous study embedded a spiking network for BG regions inside a neural field model for the cortex (Kerr et al., 2013). However, this previous modeling strategy did not subdivide the cortex mean-field model further into separate regions nor did the authors simulate DBS.

Compared to spiking models that encompass the BG regions only, our presented model can show whole-brain effects of stimulation going beyond the motor cortex. The presented results show an increase in overall activity in cortical regions for all of the three applied stimuli. This result is in line with the theory that PD patients have lower thalamic activity and, thus, a weaker driving activity from the thalamus towards the cortex. Subsequently, the cortex reacts with an increase of activity to the DBS-induced disinhibition of the thalamus. The frontal regions and the insula seem to be most impacted by all three different stimuli, measured by an increase in firing rate. The insula is linked strongly with non-motor symptoms in PD (Christopher et al., 2014) and a previous study reported a BOLD signal increase in the insula during STN-DBS (Kahan et al., 2012). The middle and inferior frontal gyrus also demonstrated one of the biggest shifts between DBS-OFF and DBS-ON condition measuring fMRI (Saenger et al., 2017). Interestingly, the monophasic stimulus applied on STN provoked a slight decrease of activity in the supplementary motor area in our results. This finding is in line with experimental results showing that DBS weakens excessive phase-locking interactions in the motor areas of PD patients (de Hemptinne et al., 2015). Supplementary motor areas, which are located at the transition between primary motor areas and prefrontal cortex, are involved in intentional movement initiation (Goldberg, 1985) and their impaired function is supposed to contribute to PD symptoms (Jacobs et al., 2009). Direct stimulation of supplementary motor areas with transcranial magnetic stimulation leads to improved freezing of gait symptoms in PD (Kim et al., 2018; Shirota et al., 2013), while dopaminergic medication can be related to improved supplementary motor area activation and improved motoric functions (Jenkins et al., 1992; Rascol et al., 1994). STN DBS in PD has been shown in fMRI (Stefurak et al., 2003) and positron emission tomography (Ceballos-Baumann et al., 1999) studies to activate motor as well as premotor areas, concordant with the simulated patterns in this work.

Our spiking network relies on a high level of biological realism with regards to spatio-temporal dynamics. Space refers to the fact that the spiking network receives input from different brain regions of TVB, which is closer to the reality regarding the multitude of different white matter connections between the cortex and the BG (Lenglet et al., 2012). More realistic time modeling implies the specific mean-field model dynamics that are chosen, as opposed to other studies, in which spiking networks are driven by Poisson spike trains, white noise or harmonic oscillations (Humphries et al., 2006; Park et al., 2011; Terman et al., 2002). The former approach of driving these spiking networks with noise seems to be an abstract view of the biologically underlying phenomena (Kerr et al., 2013).

There are still several open challenges in the field of DBS research that a virtual testing environment could potentially address. First, the exact placement of the electrodes seems crucial for the clinical outcome for patients. For PD and OCD, recent studies have shown that the connectivity profile of the brain area encompassing the inserted electrode predicts clinical outcome measures for patients (Baldermann et al., 2019; Horn et al., 2017, 2019; Joutsa et al., 2018). This phenomenon was validated for dystonia (Corp et al., 2019; Okromelidze et al., 2020), essential tremor (Al-Fatly et al., 2019) and epilepsy (Middlebrooks et al., 2018). Testing the effects of different placement strategies before surgery could provide simulation-based advice for neurosurgeons. In this first co-simulation approach for DBS, we modeled stimuli targeting the GPi or STN area directly and completely. The clinical reality looks more complex (Krauss et al., 2021) with different effects on the different neurons inside the target area. Although many complex mechanisms of DBS are known, most computational studies stay with highly simplified implementations (e.g., (Frank et al., 2007; Kumar et al., 2011; Neumann et al., 2018; Rubin and Terman, 2004). Moreover, the different sub-areas within the STN, for example, are involved in different pathways, i.e., the sensorimotor, associative and limbic loop. As most DBS systems provide several lead contacts to choose from, the precise stimulus location is a common problem in clinical fine-tuning of DBS. With the upcoming of more detailed brain atlases, one could easily extend our used parcellation towards a finer grid inside the BG and model these subparts separately. Here, we presented the scaffold model that can be fine-tuned towards a more realistic model in a straight-forward manner. Second, so far, little individual information is considered for each patient and often the electrodes are placed based on normative data (Horn and Fox, 2020). Fitting an individual TVB model for patients provides a more personalized approach based on individual structural and functional imaging or electrophysiological data. TVB has previously been applied to help with predictions of clinical features for individual patients. Using individual positron emission tomography images, EEG slowing in patients with AD could be inferred from *Abeta* accumulation with the help of TVB (Stefanovski et al., 2019). Recently, a study has shown that the TVB feature of simulated mean local field potential frequency per brain region significantly improves the classification of individuals as AD patients, mild cognitive impairment patients or healthy controls using machine learning (Triebkorn et al., 2021). For epilepsy patients, TVB has successfully been applied to optimize the determination of the resection and epileptic zone per individual before surgery (An et al., 2019).

A personalized virtual brain including structural data and dynamics based on MRI data is flexible in exploring other neuromodulation techniques with little extra effort. The hypothesis is that neuromodulation techniques can move the brain network dynamics between the diseased and healthy state (Fig. 10). With the current study, we have made a first attempt to "control" brain network dynamics by modeling stimulation in the brain of a PD patient. There is evidence that PD patients could also benefit from other neuromodulation techniques (Brittain and Cagnan, 2018). For example, a first study found that transcranial magnetic stimulation (TMS) of the supplementary motor area helps to improve the motoric symptoms of PD patients (Shirota et al., 2013). With our co-simulation framework, we can potentially analyze the impact of such a stimulation originating on the surface and follow the complete loop of cortico-basal-ganglia-thalamic-cortex connectivity. The flexibility of the presented virtual model could help with finding the best therapy for each individual patient.

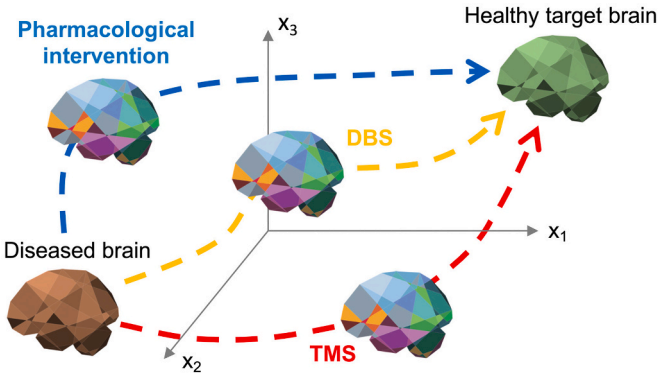

Fig. 10. Schematic overview of "controlling" brain dynamics from one state to another using The Virtual Brain. Different interventions, e.g., deep brain stimulation (DBS), transcranial magnetic stimulation (TMS) or pharmacological interventions, can shift the brain dynamics from one state to another. These neuromodulation techniques hold the potential to alter the brain dynamics from a diseased brain towards a healthy target brain. Using The Virtual Brain, we aim to explore the different pathways leading to healthy functioning in a virtual environment for individual patients.

The applied data-driven model from Maith et al. (2021) does not make use of any prior assumptions regarding the pathological PD activity within the BG network, which stands in contrast to many previous models (Leblois et al., 2006; Lindahl and Hellgren Kotaleski, 2016). Fitting the outcomes of a model with empirical data from patients and controls offers an alternative approach to determining BG and whole-brain model dynamics. With this primarily data-driven approach, Maith et al. (2021) found many similarities of the obtained personal models of individual PD patients with physiological findings of PD, such as lower firing rates in the thalamus.

Our study inherits some limitations. In this proof-of-concept study, we modeled the TVB input that drives the spiking BG network with the reduced Wong-Wang mean-field model (Deco et al., 2013). In an improved version of this model, we could adjust the TVB mean-field dynamics to qualitatively correspond better with the original spiking network of Izhikevich neurons (Maith et al., 2021) by taking advantage of existing mean-field approximations of such networks (Nicola and Campbell, 2013; Visser and Van Gils, 2014). In the same manner, the reduced Wong-Wang model is derived from Leaky Integrate-and-Fire (LIF) neurons and one could also choose to use the LIF neuronal model for the spiking dynamics to better correspond with the reduced Wong-Wang mean-field model. The current difference between the cortical input represented by an excitatory and an inhibitory population in the only-spiking network and by excitatory populations in the mean-field model could also probably be improved by a more concurrent modeling choice between the two scales. Such choices would allow a more accurate analytical and computational determination of the large-scale brain dynamics (e.g., involved bifurcations) and inform the interface modeling between the two scales accordingly (e.g., in terms of scaling or more complex transformations). Further, alternatives to correlated spike trains' generators for converting the TVB mean-field nodes' rates into spike trains of TVB "proxy" nodes could be more effective in mimicking the Izhikevich spiking cortex node dynamics. All of the above options can be better explored by an upcoming computationally optimized version of the TVB-multiscale toolbox, implementing parallel co-simulation, allowing for a systematic exploration of the parameter space of the multiscale model to better fit individual neuroimaging data. So far, we fitted the virtual co-simulation brains to two individuals, which can be easily extended to larger cohorts with the only

necessary data being DTI and either fMRI or electrophysiological data to fit the model dynamics accurately. Using the Petersen et al. (2019) atlas for the connectivity between the BG and the cortex provided us with a high resolution for these connections but lacked cortico-cortical connectivity (represented by disconnected regions in the used connectome), which is important for further propagating the stimulus effects towards other cortical areas. Future work should also include high-resolution cortico-cortical connectivity and merge it with the Petersen et al. (2019) data. Moreover, the currently used parcellation of the AAL for the cortical regions should be updated by a more detailed one, e.g. by the Glasser parcellation (Glasser et al., 2016). We ran our simulations including the isolated regions, which cost us unnecessary computational power. In future studies with larger cohorts, these isolated regions should be left out of the simulation. The regional firing rates are highly influenced by the degree in our current implementation and therefore vary quite strongly among regions (Supplementary Fig. 3). Future work should include an implementation of feedback inhibition control to counteract this (Deco et al., 2014; Schirner et al., 2018). The well-known characteristic of PD patients to demonstrate hyper-synchronization in the beta band ($8 - 35\ Hz$) in the sensorimotor network and the STN (Cruz et al., 2011; Whitmer et al., 2012) is reversed by DBS (Kühn et al., 2008; Wingeier et al., 2006). Our approach did not yet incorporate modeling the electrophysiological signatures of virtual DBS. However, one strength of the current model is the necessary data availability since it only requires fMRI data. It would be clearly more efficient to directly use electrophysiological data, e.g. EEG or local field potentials, to tune such models, but the corresponding data is often not available, especially in humans. In addition, the influence of neurovascular coupling on the forward model to derive BOLD signals is still unclear (Maith et al., 2022). Therefore, we plan to include LFP recordings of DBS electrodes during optimization, which are often available in PD patients. Combining all available data will certainly be the goal of future research applying these models. Short-term plasticity probably plays an essential role in DBS effects (Milosevic et al., 2018), which has not yet been implemented in our model. Similarly, long-term plasticity effects due to DBS probably exist in structural and functional networks (van Hartevelt et al., 2014). With the spiking model allowing for an implementation of plasticity rules, we could explore its effects on the whole-brain dynamics with our model in future work. Moreover, our BG network misses the substantia nigra region as a crucial factor influencing PD dynamics and so far, we limited our analyses to a single (left) hemisphere.

5. Conclusions

In this study, we presented a co-simulation model for the BG as a spiking network together with TVB mean-field simulations for the whole brain. Our results show biologically plausible effects of virtual DBS performed in this multiscale modeling framework, bringing the patient's network dynamics of the BG closer to the healthy regime. The presented model offers a bridge between the different scales affected by DBS in the brain. It has the potential to be used as a 'sandbox' model for individual patients suffering from different neurological disorders prior to surgical interventions. Different strategies for DBS lead placements and configurations can be tested and evaluated. Future work needs to validate this model in larger patient cohorts and establish its link with clinical post-surgery improvement.

Declaration of Competing Interest

The authors declare that they have no known competing financial interests or personal relationships that could have appeared to influence the work reported in this paper.

Acknowledgments

PR acknowledges support by EU H2020 Virtual Brain Cloud 826421, Human Brain Project SGA2 785907; Human Brain Project SGA3 945539, ERC Consolidator 683049; German Research Foundation SFB 1436 (project ID 425899996); SFB 1315 (project ID 327654276); SFB 936 (project ID 178316478); SFB-TRR 295 (project ID 424778381); SPP Computational Connectomics RI 2073/6-1, RI 2073/10-2, RI 2073/9-1; Berlin Institute of Health & Foundation Charité, Johanna Quandt Excellence Initiative. In addition, we acknowledge support from the German Research Foundation (DFG) HA2630/11-1 and HA2630/11-2 part of "Computational Connectomics" (SPP 2041) and the Open Access Publication Fund of Charité-Universitätsmedizin Berlin. We thank Ningfei Li, Simón Oxenford and Andreas Horn for helping us prepare the connectome data for TVB and being involved in initial discussions. We are grateful to Julien Vitay for providing us with guidance concerning the usage of ANNarchy and being involved in initial discussions. We thank Arjan Hillebrand for sharing his code to visualize the template brains with us.

Appendix A. Supplementary data

Supplementary data to this article can be found online at https://doi.org/10.1016/j.expneurol.2022.114111.

References

Abecassis, Z.A., Berceau, B.L., Win, P.H., García, D., Xenias, H.S., Cui, Q., Pamukcu, A., Cherian, S., Hernández, V.M., Chon, U., Lim, B.K., Kim, Y., Justice, N.J., Awatramani, R., Hooks, B.M., Gerfen, C.R., Boca, S.M., Chan, C.S., 2020. Npas1-Nkx2.1 neurons are an integral part of the cortico-pallido-cortical loop. J. Neurosci. 40 (4), 743–768. https://doi.org/10.1523/JNEUROSCI.1199-19.2019.

Ackermans, L., Duits, A., van der Linden, C., Tijssen, M., Schruers, K., Temel, Y., Kleijer, M., Nederveen, P., Bruggeman, R., Tromp, S., van Kranen-Mastenbroek, V., Kingma, H., Cath, D., Visser-Vandewalle, V., 2011. Double-blind clinical trial of thalamic stimulation in patients with Tourette syndrome. Brain 134 (3), 832–844. https://doi.org/10.1093/brain/awq380.

Aerts, H., Schirner, M., Jeurissen, B., Van Roost, D., Achten, E., Ritter, P., Marinazzo, D., 2018. Modeling brain dynamics in brain tumor patients using The Virtual Brain. eNeuro 5 (3). https://doi.org/10.1523/ENEURO.0083-18.2018.

Albin, R.L., Young, A.B., Penney, J.B., 1989. The functional anatomy of basal ganglia disorders. Trends Neurosci. 12 (10), 366–375. https://doi.org/10.1016/0166-2236(89)90074-x.

Al-Fatly, B., Ewert, S., Kübler, D., Kroneberg, D., Horn, A., Kühn, A.A., 2019. Connectivity profile of thalamic deep brain stimulation to effectively treat essential tremor. Brain 142 (10), 3086–3098.

An, S., Bartolomei, F., Guye, M., Jirsa, V., 2019. Optimization of surgical intervention outside the epileptogenic zone in the Virtual Epileptic Patient (VEP). PLoS Comput. Biol. 15 (6), e1007051 https://doi.org/10.1371/journal.pcbi.1007051.

Anderson, D., Ahmed, A., 2003. Treatment of patients with intractable obsessive-compulsive disorder with anterior capsular stimulation. Case report. J. Neurosurg. 98 (5), 1104–1108. https://doi.org/10.3171/jns.2003.98.5.1104.

Baladron, J., Hamker, F.H., 2020. Habit learning in hierarchical cortex-basal ganglia loops. Eur. J. Neurosci. 52 (12), 4613–4638. https://doi.org/10.1111/ejn.14730.

Baladron, J., Nambu, A., Hamker, F.H., 2019. The subthalamic nucleus-external globus pallidus loop biases exploratory decisions towards known alternatives: a neuro-computational study. Eur. J. Neurosci. 49 (6), 754–767. https://doi.org/10.1111/ejn.13666.

Baldermann, J.C., Melzer, C., Zapf, A., Kohl, S., Timmermann, L., Tittgemeyer, M., Huys, D., Visser-Vandewalle, V., Kühn, A.A., Horn, A., Kuhn, J., 2019. Connectivity profile predictive of effective deep brain stimulation in obsessive-compulsive disorder. Biol. Psychiatry 85 (9), 735–743. https://doi.org/10.1016/j.biopsych.2018.12.019.

Benazzouz, A., Piallat, B., Pollak, P., Benabid, A.L., 1995. Responses of substantia nigra pars reticulata and globus pallidus complex to high frequency stimulation of the subthalamic nucleus in rats: electrophysiological data. Neurosci. Lett. 189 (2), 77–80. https://doi.org/10.1016/s0306-4522(00)00199-8.

Benazzouz, A., Gao, D.M., Ni, Z.G., Piallat, B., Bouali-Benazzouz, R., Benabid, A.L., 2000. Effect of high-frequency stimulation of the subthalamic nucleus on the neuronal activities of the substantia nigra pars reticulata and ventrolateral nucleus of the thalamus in the rat. Neuroscience 99 (2), 289–295. https://doi.org/10.1016/0304-3940(95)11455-6.

Bergelt, J., Hamker, F.H., 2019. Spatial updating of attention across eye movements: a neuro-computational approach. J. Vis. 19 (7), 10. https://doi.org/10.1167/19.7.10.

Brittain, J.-S., Cagnan, H., 2018. Recent trends in the use of electrical neuromodulation in Parkinson's Disease. Curr. Behav. Neurosci. Rep. 5 (2), 170–178. https://doi.org/10.1007/s40473-018-0154-9.

Ceballos-Baumann, A.O., Boecker, H., Bartenstein, P., von Falkenhayn, I., Riescher, H., Conrad, B., Moringlane, J.R., Alesch, F., 1999. A positron emission tomographic study of subthalamic nucleus stimulation in Parkinson disease: enhanced movement-related activity of motor-association cortex and decreased motor cortex resting

activity. Arch. Neurol. 56 (8), 997–1003. https://doi.org/10.1001/archneur.56.8.997.
Chen, M.C., Ferrari, L., Sacchet, M.D., Foland-Ross, L.C., Qiu, M.-H., Gotlib, I.H., Fuller, P.M., Arrigoni, E., Lu, J., 2015. Identification of a direct GABAergic pallidocortical pathway in rodents. Eur. J. Neurosci. 41 (6), 748–759. https://doi.org/10.1111/ejn.12822.
Chiken, S., Nambu, A., 2016. Mechanism of deep brain stimulation: inhibition, excitation, or disruption? Neuroscientist 22 (3), 313–322. https://doi.org/10.1177/1073858415581986.
Christopher, L., Koshimori, Y., Lang, A.E., Criaud, M., Strafella, A.P., 2014. Uncovering the role of the insula in non-motor symptoms of Parkinson's disease. Brain 137 (8), 2143–2154. https://doi.org/10.1093/brain/awu084.
Corp, D.T., Joutsa, J., Darby, R.R., Delnooz, C.C.S., van de Warrenburg, B.P.C., Cooke, D., Prudente, C.N., Ren, J., Reich, M.M., Batla, A., Bhatia, K.P., Jinnah, H.A., Liu, H., Fox, M.D., 2019. Network localization of cervical dystonia based on causal brain lesions. Brain 142 (6), 1660–1674. https://doi.org/10.1093/brain/awz112.
Cruz, A.V., Mallet, N., Magill, P.J., Brown, P., Averbeck, B.B., 2011. Effects of dopamine depletion on information flow between the subthalamic nucleus and external globus pallidus. J. Neurophysiol. 106 (4), 2012–2023. https://doi.org/10.1152/jn.00094.2011.
Cui, Q., Pamukcu, A., Cherian, S., Chang, I.Y.M., Berceau, B.L., Xenias, H.S., Higgs, M.H., Rajamanickam, S., Chen, Y., Du, X., Zhang, Y., McMorrow, H., Abecassis, Z.A., Boca, S.M., Justice, N.J., Wilson, C.J., Chan, C.S., 2021. Dissociable roles of pallidal neuron subtypes in regulating motor patterns. J. Neurosci. 41 (18), 4036–4059. https://doi.org/10.1523/JNEUROSCI.2210-20.2021.
Damier, P., Hirsch, E.C., Agid, Y., Graybiel, A.M., 1999. The substantia nigra of the human brain. II. Patterns of loss of dopamine-containing neurons in Parkinson's disease. Brain 122 (8), 1437–1448. https://doi.org/10.1093/brain/122.8.1437.
de Hemptinne, C., Swann, N.C., Ostrem, J.L., Ryapolova-Webb, E.S., San Luciano, M., Galifianakis, N.B., Starr, P.A., 2015. Therapeutic deep brain stimulation reduces cortical phase-amplitude coupling in Parkinson's disease. Nat. Neurosci. 18 (5), 779–786. https://doi.org/10.1038/nn.3997.
Deco, G., Ponce-Alvarez, A., Mantini, D., Romani, G.L., Hagmann, P., Corbetta, M., 2013. Resting-state functional connectivity emerges from structurally and dynamically shaped slow linear fluctuations. J. Neurosci. 33 (27), 11239–11252. https://doi.org/10.1523/JNEUROSCI.1091-13.2013.
Deco, G., Ponce-Alvarez, A., Hagmann, P., Romani, G.L., Mantini, D., Corbetta, M., 2014. How local excitation-inhibition ratio impacts the whole brain dynamics. J. Neurosci. 34 (23), 7886–7898. https://doi.org/10.1523/jneurosci.5068-13.2014.
DeLong, M.R., 1990. Primate models of movement disorders of basal ganglia origin. Trends Neurosci. 13 (7), 281–285. https://doi.org/10.1016/0166-2236(90)90110-v.
Deuschl, G., Schade-Brittinger, C., Krack, P., Volkmann, J., Schäfer, H., Bötzel, K., Daniels, C., Deutschländer, A., Dillmann, U., Eisner, W., Gruber, D., Hamel, W., Herzog, J., Hilker, R., Klebe, S., Kloß, M., Koy, J., Krause, M., Kupsch, A., Voges, J., 2006. A randomized trial of deep-brain stimulation for Parkinson's Disease. N. Engl. J. Med. 355 (9), 896–908. https://doi.org/10.1056/nejmoa060281.
Dostrovsky, J.O., Hutchison, W.D., Lozano, A.M., 2002. The globus pallidus, deep brain stimulation, and Parkinson's disease. Neuroscientist 8 (3), 284–290. https://doi.org/10.1177/1073858402008003014.
Eisinger, R.S., Cernera, S., Gittis, A., Gunduz, A., Okun, M.S., 2019. A review of basal ganglia circuits and physiology: application to deep brain stimulation. Parkinsonism Relat. Disord. 59, 9. https://doi.org/10.1016/j.parkreldis.2019.01.009.
Eppler, J.M., Helias, M., Muller, E., Diesmann, M., Gewaltig, M.-O., 2008. PyNEST: a convenient Interface to the NEST simulator. Front. Neuroinforma. 2, 12. https://doi.org/10.3389/neuro.11.012.2008.
Fearnley, J.M., Lees, A.J., 1991. Ageing and Parkinson's disease: substantia nigra regional selectivity. Brain 114 (5), 2283–2301. https://doi.org/10.1093/brain/114.5.2283.
Frank, M.J., Samanta, J., Moustafa, A.A., Sherman, S.J., 2007. Hold your horses: impulsivity, deep brain stimulation, and medication in parkinsonism. Science 318 (5854), 1309–1312. https://doi.org/10.1126/science.1146157.
Franzini, A., Messina, G., Gambini, O., Muffatti, R., Scarone, S., Cordella, R., Broggi, G., 2010. Deep-brain stimulation of the nucleus accumbens in obsessive compulsive disorder: clinical, surgical and electrophysiological considerations in two consecutive patients. Neurol. Sci. 31 (3), 353–359. https://doi.org/10.1007/s10072-009-0214-8.
Glasser, M.F., Coalson, T.S., Robinson, E.C., Hacker, C.D., Harwell, J., Yacoub, E., Ugurbil, K., Andersson, J., Beckmann, C.F., Jenkinson, M., Smith, S.M., Van Essen, D. C., 2016. A multi-modal parcellation of human cerebral cortex. Nature 536 (7615), 171–178. https://doi.org/10.1038/nature18933.
Goldberg, G., 1985. Supplementary motor area structure and function: review and hypotheses. Behav. Brain Sci. 8 (4), 567–588. https://doi.org/10.1017/s0140525x00045167.
Gönner, L., Vitay, J., Hamker, F.H., 2017. Predictive place-cell sequences for goal-finding emerge from goal memory and the cognitive map: a computational model. Front. Comput. Neurosci. 11, 84. https://doi.org/10.3389/fncom.2017.00084.
Gönner, L., Maith, O., Koulouri, I., Baladron, J., Hamker, F.H., 2020. A spiking model of basal ganglia dynamics in stopping behavior supported by arkypallidal neurons. Eur. J. Neurosci. https://doi.org/10.1111/ejn.15082.
Gruber, D., Kuhn, A.A., Schoenecker, T., Kopp, U.A., Kivi, A., Huebl, J., Lobsien, E., Mueller, B., Schneider, G.-H., Kupsch, A., 2014. Quadruple deep brain stimulation in Huntington's disease, targeting pallidum and subthalamic nucleus: case report and review of the literature. J. Neural Transm. 121 (10), 1303–1312. https://doi.org/10.1007/s00702-014-1201-7.
Guo, Y., Rubin, J.E., McIntyre, C.C., Vitek, J.L., Terman, D., 2008. Thalamocortical relay fidelity varies across subthalamic nucleus deep brain stimulation protocols in a data-driven computational model. J. Neurophysiol. 99 (3), 1477–1492. https://doi.org/10.1152/jn.01080.2007.
Heimer, L., 1983. Basal Ganglia. In: The Human Brain and Spinal Cord. Springer, New York, NY, pp. 199–209. https://doi.org/10.1007/978-1-4684-0150-9_15.
Horn, A., 2019. The impact of modern-day neuroimaging on the field of deep brain stimulation. Curr. Opin. Neurol. 32 (4), 511–520. https://doi.org/10.1097/WCO.0000000000000679.
Horn, A., Fox, M.D., 2020. Opportunities of connectomic neuromodulation. NeuroImage 221, 117180. https://doi.org/10.1016/j.neuroimage.2020.117180.
Horn, A., Kühn, A.A., 2015. Lead-DBS: a toolbox for deep brain stimulation electrode localizations and visualizations. NeuroImage 107, 127–135. https://doi.org/10.1016/j.neuroimage.2014.12.002.
Horn, A., Reich, M., Vorwerk, J., Li, N., Wenzel, G., Fang, Q., Schmitz-Hübsch, T., Nickl, R., Kupsch, A., Volkmann, J., Kühn, A.A., Fox, M.D., 2017. Connectivity predicts deep brain stimulation outcome in Parkinson disease. Ann. Neurol. 82 (1), 67–78. https://doi.org/10.1002/ana.24974.
Horn, A., Wenzel, G., Irmen, F., Huebl, J., Li, N., Neumann, W.-J., Krause, P., Bohner, G., Scheel, M., Kühn, A.A., 2019. Deep brain stimulation induced normalization of the human functional connectome in Parkinson's disease. Brain 142 (10), 3129–3143. https://doi.org/10.1093/brain/awz239.
Humphries, M.D., Stewart, R.D., Gurney, K.N., 2006. A physiologically plausible model of action selection and oscillatory activity in the basal ganglia. J. Neurosci. 26 (50), 12921–12942. https://doi.org/10.1523/JNEUROSCI.3486-06.2006.
Humphries, M.D., Obeso, J.A., Dreyer, J.K., 2018. Insights into Parkinson's disease from computational models of the basal ganglia. J. Neurol. Neurosurg. Psychiatry 89 (11), 1181–1188. https://doi.org/10.1136/jnnp-2017-315922.
Irmen, F., Horn, A., Meder, D., Neumann, W.-J., Plettig, P., Schneider, G.-H., Siebner, H. R., Kühn, A.A., 2019. Sensorimotor subthalamic stimulation restores risk-reward trade-off in Parkinson's disease. Movement Disorders 34 (3), 366–376. https://doi.org/10.1002/mds.27576.
Izhikevich, E.M., 2004. Which model to use for cortical spiking neurons? IEEE Trans. Neural Networks Publ. IEEE Neural Networks Council 15 (5), 1063–1070. https://doi.org/10.1109/TNN.2004.832719.
Jacobs, J.V., Lou, J.S., Kraakevik, J.A., Horak, F.B., 2009. The supplementary motor area contributes to the timing of the anticipatory postural adjustment during step initiation in participants with and without Parkinson's disease. Neuroscience 164 (2), 877–885. https://doi.org/10.1016/j.neuroscience.2009.08.002.
Jahanshahi, M., Obeso, I., Baunez, C., Alegre, M., Krack, P., 2015. Parkinson's disease, the subthalamic nucleus, inhibition, and impulsivity. Movement Disorders 30 (2), 128–140. https://doi.org/10.1002/mds.26049.
Jamalian, A., Bergelt, J., Dinkelbach, H.Ü., Hamker, F.H., 2017. Spatial attention improves object localization: a biologically plausible neuro-computational model for use in virtual reality. IEEE Int. Conf. Computer Vision Workshops (ICCVW) 2017, 2724–2729. https://doi.org/10.1109/ICCVW.2017.320.
Jech, R., Urgosík, D., Tintera, J., Nebuzelský, A., Krásenský, J., Liscák, R., Roth, J., Ruzicka, E., 2001. Functional magnetic resonance imaging during deep brain stimulation: a pilot study in four patients with Parkinson's disease. Movement Disorders 16 (6), 1126–1132. https://doi.org/10.1002/mds.1217.
Jenkins, I.H., Fernandez, W., Playford, E.D., Lees, A.J., Frackowiak, R.S., Passingham, R. E., Brooks, D.J., 1992. Impaired activation of the supplementary motor area in Parkinson's disease is reversed when akinesia is treated with apomorphine. Ann. Neurol. 32 (6), 749–757. https://doi.org/10.1002/ana.410320608.
Jones, D.K., Knösche, T.R., Turner, R., 2013. White matter integrity, fiber count, and other fallacies: the do's and don'ts of diffusion MRI. NeuroImage 73, 239–254. https://doi.org/10.1016/j.neuroimage.2012.06.081.
Joutsa, J., Horn, A., Hsu, J., Fox, M.D., 2018. Localizing parkinsonism based on focal brain lesions. Brain 141 (8), 2445–2456. https://doi.org/10.1093/brain/awy161.
Kahan, J., Mancini, L., Urner, M., Friston, K., Hariz, M., Holl, E., White, M., Ruge, D., Jahanshahi, M., Boertien, T., Yousry, T., Thornton, J.S., Limousin, P., Zrinzo, L., Foltynie, T., 2012. Therapeutic subthalamic nucleus deep brain stimulation reverses cortico-thalamic coupling during voluntary movements in Parkinson's disease. PLoS One 7 (12), e50270. https://doi.org/10.1371/journal.pone.0050270.
Kerr, C.C., Van Albada, S.J., Neymotin, S.A., Chadderdon, G.L., Robinson, P.A., Lytton, W.W., 2013. Cortical information flow in Parkinson's disease: a composite network/field model. Front. Comput. Neurosci. 7, 39. https://doi.org/10.3389/fncom.2013.00039.
Kim, S.J., Paeng, S.H., Kang, S.Y., 2018. Stimulation in supplementary motor area versus motor cortex for freezing of gait in Parkinson's disease. J. Clin. Neurol. 14 (3), 320–326. https://doi.org/10.3988/jcn.2018.14.3.320.
Klein, P.C., Ettinger, U., Schirner, M., Ritter, P., Rujescu, D., Falkai, P., Koutsouleris, N., Kambeitz-Ilankovic, L., Kambeitz, J., 2021. Brain network simulations indicate effects of Neuregulin-1 genotype on excitation-inhibition balance in cortical dynamics. Cereb. Cortex 31 (4), 2013–2025. https://doi.org/10.1093/cercor/bhaa339.
Koller, W., Pahwa, R., Busenbark, K., Hubble, J., Wilkinson, S., Lang, A., Tuite, P., Sime, E., Lazano, A., Hauser, R., Malapira, T., Smith, D., Tarsy, D., Miyawaki, E., Norregaard, T., Kormos, T., Olanow, C.W., 1997. High-frequency unilateral thalamic stimulation in the treatment of essential and parkinsonian tremor. Ann. Neurol. 42 (3), 292–299. https://doi.org/10.1002/ana.410420304.
Krauss, J.K., Lipsman, N., Aziz, T., Boutet, A., Brown, P., Chang, J.W., Davidson, B., Grill, W.M., Hariz, M.I., Horn, A., Schulder, M., Mammis, A., Tass, P.A., Volkmann, J., Lozano, A.M., 2021. Technology of deep brain stimulation: current status and future directions. Nat. Rev. Neurol. 17 (2), 75–87. https://doi.org/10.1038/s41582-020-00426-z.
Kühn, A.A., Kempf, F., Brücke, C., Gaynor Doyle, L., Martinez-Torres, I., Pogosyan, A., Trottenberg, T., Kupsch, A., Schneider, G.-H., Hariz, M.I., Vandenberghe, W.,

Nuttin, B., Brown, P., 2008. High-frequency stimulation of the subthalamic nucleus suppresses oscillatory beta activity in patients with Parkinson's disease in parallel with improvement in motor performance. J. Neurosci. 28 (24), 6165–6173. https://doi.org/10.1523/JNEUROSCI.0282-08.2008.

Kumar, A., Cardanobile, S., Rotter, S., Aertsen, A., 2011. The role of inhibition in generating and controlling Parkinson's disease oscillations in the basal ganglia. Front. Syst. Neurosci. 5, 86. https://doi.org/10.3389/fnsys.2011.00086.

Kunze, T., Hunold, A., Haueisen, J., Jirsa, V., Spiegler, A., 2016. Transcranial direct current stimulation changes resting state functional connectivity: a large-scale brain network modeling study. NeuroImage 140, 174–187. https://doi.org/10.1016/j.neuroimage.2016.02.015.

Kupsch, A., Benecke, R., Müller, J., Trottenberg, T., Schneider, G.-H., Poewe, W., Eisner, W., Wolters, A., Müller, J.-U., Deuschl, G., Pinsker, M.O., Skogseid, I.M., Roeste, G.K., Vollmer-Haase, J., Brentrup, A., Krause, M., Tronnier, V., Schnitzler, A., Voges, J., Volkmann, J., 2006. Pallidal deep-brain stimulation in primary generalized or segmental dystonia. N. Engl. J. Med. 355 (19), 1978–1990. https://doi.org/10.1056/nejmoa063618.

Lanciego, J.L., Luquin, N., Obeso, J.A., 2012. Functional neuroanatomy of the basal ganglia. Cold Spring Harbor Perspect. Med. 2 (12) https://doi.org/10.1101/cshperspect.a009621.

Larisch, R., Gönner, L., Teichmann, M., Hamker, F.H., 2021. Sensory coding and contrast invariance emerge from the control of plastic inhibition over excitatory connectivity. PLoS Computational Biology 17 (11), e1009566. https://doi.org/10.1101/2020.04.07.029157.

Leblois, A., Boraud, T., Meissner, W., Bergman, H., Hansel, D., 2006. Competition between feedback loops underlies normal and pathological dynamics in the basal ganglia. J. Neurosci. 26 (13), 3567–3583. https://doi.org/10.1523/JNEUROSCI.5050-05.2006.

Lenglet, C., Abosch, A., Yacoub, E., De Martino, F., Sapiro, G., Harel, N., 2012. Comprehensive in vivo mapping of the human basal ganglia and thalamic connectome in individuals using 7T MRI. PLoS One 7 (1), e29153. https://doi.org/10.1371/journal.pone.0029153.

Lindahl, M., Hellgren Kotaleski, J., 2016. Untangling basal ganglia network dynamics and function: role of dopamine depletion and inhibition investigated in a spiking network model. eNeuro 3 (6). https://doi.org/10.1523/ENEURO.0156-16.2016.

Liu, C., Zhao, G., Wang, J., Wu, H., Li, H., Fietkiewicz, C., Loparo, K.A., 2020. Neural network-based closed-loop deep brain stimulation for modulation of pathological oscillation in Parkinson's disease. IEEE Access 8, 161067–161079. https://doi.org/10.3389/fninf.2022.790966.

Maith, O., Villagrasa Escudero, F., Dinkelbach, H.Ü., Baladron, J., Horn, A., Irmen, F., Kühn, A.A., Hamker, F.H., 2021. A computational model-based analysis of basal ganglia pathway changes in Parkinson's disease inferred from resting-state fMRI. Eur. J. Neurosci. 53 (7), 2278–2295. https://doi.org/10.1111/ejn.14868.

Maith, O., Dinkelbach, H.Ü., Baladron, J., Vitay, J., Hamker, F.H., 2022. BOLD monitoring in the neural simulator ANNarchy. Front. Neuroinforma. https://doi.org/10.3389/fninf.2022.790966.

Marsden, C.D., Obeso, J.A., 1994. The functions of the basal ganglia and the paradox of stereotaxic surgery in Parkinson's disease. Brain 117 (4), 877–897. https://doi.org/10.1093/brain/117.4.877.

Mayberg, H.S., Lozano, A.M., Voon, V., McNeely, H.E., Seminowicz, D., Hamani, C., Schwalb, J.M., Kennedy, S.H., 2005. Deep brain stimulation for treatment-resistant depression. Neuron 45 (5), 651–660. https://doi.org/10.1016/j.neuron.2005.02.014.

Michmizos, K.P., Nikita, K.S., 2011. Addition of deep brain stimulation signal to a local field potential driven Izhikevich model masks the pathological firing pattern of an STN neuron. In: Conference Proceedings of 2011 Annual International Conference of the IEEE Engineering in Medicine and Biology Society, pp. 7290–7293. https://doi.org/10.1109/IEMBS.2011.6091700. https://ieeexplore.ieee.org/abstract/document/6091700.

Middlebrooks, E.H., Grewal, S.S., Stead, M., Lundstrom, B.N., Worrell, G.A., Van Gompel, J.J., 2018. Differences in functional connectivity profiles as a predictor of response to anterior thalamic nucleus deep brain stimulation for epilepsy: a hypothesis for the mechanism of action and a potential biomarker for outcomes. Neurosurg. Focus. 45 (2), E7. https://doi.org/10.3171/2018.5.FOCUS18151.

Milosevic, L., Kalia, S.K., Hodaie, M., Lozano, A.M., Fasano, A., Popovic, M.R., Hutchison, W.D., 2018. Neuronal inhibition and synaptic plasticity of basal ganglia neurons in Parkinson's disease. Brain 141 (1), 177–190. https://doi.org/10.1093/brain/awx296.

Mueller, K., Jech, R., Ružicka, F., Holiga, Š., Ballarini, T., Bezdicek, O., Möller, H.E., Vymazal, J., Ružicka, E., Schroeter, M.L., Urgošík, D., 2018. Brain connectivity changes when comparing effects of subthalamic deep brain stimulation with levodopa treatment in Parkinson's disease. NeuroImage Clincal 19. https://doi.org/10.1016/j.nicl.2018.05.006.

Müller, U.J., Sturm, V., Voges, J., Heinze, H.-J., Galazky, I., Heldmann, M., Scheich, H., Bogerts, B., 2009. Successful treatment of chronic resistant alcoholism by deep brain stimulation of nucleus accumbens: first experience with three cases. Pharmacopsychiatry 42 (6), 288–291. https://doi.org/10.1055/s-0029-1233489.

Müller, J., Nawrot, M., Menzel, R., Landgraf, T., 2018. A neural network model for familiarity and context learning during honeybee foraging flights. Biol. Cybern. 112 (1–2), 113–126. https://doi.org/10.1007/s00422-017-0732-z.

Neumann, W.-J., Schroll, H., de Almeida Marcelino, A.L., Horn, A., Ewert, S., Irmen, F., Krause, P., Schneider, G.-H., Hamker, F., Kühn, A.A., 2018. Functional segregation of basal ganglia pathways in Parkinson's disease. Brain 141 (9), 2655–2669. https://doi.org/10.1093/brain/awy206.

Nicola, W., Campbell, S.A., 2013. Mean-field models for heterogeneous networks of two-dimensional integrate and fire neurons. Front. Comput. Neurosci. 7 https://doi.org/10.3389/fncom.2013.00184.

Noecker, A.M., Frankemolle-Gilbert, A.M., Howell, B., Petersen, M.V., Beylergil, S.B., Shaikh, A.G., McIntyre, C.C., 2021. StimVision v2: examples and applications in subthalamic deep brain stimulation for Parkinson's Disease. Neuromodulation 24 (2), 248–258. https://doi.org/10.1111/ner.13350.

Nuttin, B.J., Gabriëls, L.A., Cosyns, P.R., Meyerson, B.A., Andréewitch, S., Sunaert, S.G., Maes, A.F., Dupont, P.J., Gybels, J.M., Gielen, F., Demeulemeester, H.G., 2008. Long-term electrical capsular stimulation in patients with obsessive-compulsive disorder. Neurosurgery 62 (6 Suppl 3), 966–977. https://doi.org/10.1227/01.neu.0000333764.20575.d6.

Okromelidze, L., Tsuboi, T., Eisinger, R.S., Burns, M.R., Charbel, M., Rana, M., Grewal, S. S., Lu, C.-Q., Almeida, L., Foote, K.D., Okun, M.S., Middlebrooks, E.H., 2020. Functional and structural connectivity patterns associated with clinical outcomes in deep brain stimulation of the globus pallidus internus for generalized dystonia. AJNR Am. J. Neuroradiol. 41 (3), 508–514. https://doi.org/10.3174/ajnr.A6429.

Oxenford, S., Roediger, J., Milosevic, L., Güttler, C., Spindler, P., Vajkoczy, P., Neumann, W.-J., Kühn, A., Horn, A., 2021. Lead-OR: A Multimodal Platform for Deep Brain Stimulation Surgery. https://doi.org/10.1101/2021.08.09.21261792.

Park, C., Worth, R.M., Rubchinsky, L.L., 2011. Neural dynamics in parkinsonian brain: the boundary between synchronized and nonsynchronized dynamics. Phys. Rev. E Stat. Nonlinear Soft Matter Phys. 83 (4 Pt 1), 042901 https://doi.org/10.1103/PhysRevE.83.042901.

Pauli, W.M., Nili, A.N., Tyszka, J.M., 2018. A high-resolution probabilistic in vivo atlas of human subcortical brain nuclei. Scientific Data 5, 180063. https://doi.org/10.1038/sdata.2018.63.

Petersen, M.V., Mlakar, J., Haber, S.N., Parent, M., Smith, Y., Strick, P.L., Griswold, M.A., McIntyre, C.C., 2019. Holographic reconstruction of axonal pathways in the human brain. Neuron 104 (6), 1056–1064.e3. https://doi.org/10.1016/j.neuron.2019.09.030.

Plotkin, J.L., Goldberg, J.A., 2019. Thinking outside the box (and arrow): current themes in striatal dysfunction in movement disorders. Neuroscientist 25 (4), 359–379. https://doi.org/10.1177/1073858418807887.

Rascol, O., Sabatini, U., Chollet, F., Fabre, N., Senard, J.M., Montastruc, J.L., Celsis, P., Marc-Vergnes, J.P., Rascol, A., 1994. Normal activation of the supplementary motor area in patients with Parkinson's disease undergoing long-term treatment with levodopa. J. Neurol. Neurosurg. Psychiatry 57 (5), 567–571. https://doi.org/10.1136/jnnp.57.5.567.

Reese, R., Leblois, A., Steigerwald, F., Pötter-Nerger, M., Herzog, J., Maximilian Mehdorn, H., Deuschl, G., Meissner, W.G., Volkmann, J., 2011. Subthalamic deep brain stimulation increases pallidal firing rate and regularity. Exp. Neurol. 229 (2), 517–521. https://doi.org/10.1016/j.expneurol.2011.01.020.

Ritter, P., Schirner, M., McIntosh, A.R., Jirsa, V.K., 2013. The Virtual Brain integrates computational modeling and multimodal neuroimaging. Brain Connectivity 3 (2), 121–145. https://doi.org/10.1089/brain.2012.0120.

Rodriguez-Oroz, M.C., Jahanshahi, M., Krack, P., Litvan, I., Macias, R., Bezard, E., Obeso, J.A., 2009. Initial clinical manifestations of Parkinson's disease: features and pathophysiological mechanisms. Lancet Neurol. 8 (12), 1128–1139. https://doi.org/10.1016/S1474-4422(09)70293-5.

Rolls, E., Joliot, M., Tzourio-Mazoyer, N., 2015. Implementation of a new parcellation of the orbitofrontal cortex in the automated anatomical labeling atlas. NeuroImage 122, 1–5. https://doi.org/10.1016/j.neuroimage.2015.07.075.

Rubin, J.E., Terman, D., 2004. High frequency stimulation of the subthalamic nucleus eliminates pathological thalamic rhythmicity in a computational model. J. Comput. Neurosci. 16 (3), 211–235. https://doi.org/10.1023/b:jcns.0000025686.47117.67.

Saenger, V.M., Kahan, J., Foltynie, T., Friston, K., Aziz, T.Z., Green, A.L., van Hartevelt, T.J., Cabral, J., Stevner, A.B.A., Fernandes, H.M., Mancini, L., Thornton, J., Yousry, T., Limousin, P., Zrinzo, L., Hariz, M., Marques, P., Sousa, N., Kringelbach, M.L., Deco, G., 2017. Uncovering the underlying mechanisms and whole-brain dynamics of deep brain stimulation for Parkinson's disease. Sci. Rep. 7 (1), 9882. https://doi.org/10.1038/s41598-017-10003-y.

Salanova, V., Witt, T., Worth, R., Henry, T.R., Gross, R.E., Nazzaro, J.M., Labar, D., Sperling, M.R., Sharan, A., Sandok, E., Handforth, A., Stern, J.M., Chung, S., Henderson, J.M., French, J., Baltuch, G., Rosenfeld, W.E., Garcia, P., Barbaro, N.M., SANTE Study Group, 2015. Long-term efficacy and safety of thalamic stimulation for drug-resistant partial epilepsy. Neurology 84 (10), 1017–1025. https://doi.org/10.1212/WNL.0000000000001334.

Sanz Leon, P., Knock, S.A., Woodman, M.M., Domide, L., Mersmann, J., McIntosh, A.R., Jirsa, V., 2013. The Virtual Brain: a simulator of primate brain network dynamics. Front. Neuroinforma. 7, 10. https://doi.org/10.3389/fninf.2013.00010.

Saunders, A., Oldenburg, I.A., Berezovskii, V.K., Johnson, C.A., Kingery, N.D., Elliott, H. L., Xie, T., Gerfen, C.R., Sabatini, B.L., 2015. A direct GABAergic output from the basal ganglia to frontal cortex. Nature 521 (7550), 85–89. https://doi.org/10.1038/nature14179.

Schirner, M., McIntosh, A.R., Jirsa, V., Deco, G., Ritter, P., 2018. Inferring multi-scale neural mechanisms with brain network modelling. eLife 7. https://doi.org/10.7554/eLife.28927.

Schirner, M., Domide, L., Perdikis, D., Triebkorn, P., Stefanovski, L., Pai, R., Prodan, P., Valean, B., Palmer, J., Langford, C., Blickensdörfer, A., van der Vlag, M., Diaz-Pier, S., Peyser, A., Klijn, W., Pleiter, D., Nahm, A., Schmid, O., Woodman, M., Ritter, P., 2022. Brain simulation as a cloud service: The Virtual Brain on EBRAINS. NeuroImage 251, 118973. https://doi.org/10.1016/j.neuroimage.2022.118973.

Schmid, K., Vitay, J., Hamker, F.H., 2019. Forward models in the cerebellum using reservoirs and perturbation learning. In: 2019 Conference on Cognitive

Computational Neuroscience. 2019 Conference on Cognitive Computational Neuroscience, Berlin, Germany. https://doi.org/10.32470/ccn.2019.1139-0.
Shirota, Y., Ohtsu, H., Hamada, M., Enomoto, H., Ugawa, Y., For the Research Committee on rTMS Treatment of Parkinson's Disease, 2013. Supplementary motor area stimulation for Parkinson disease: A randomized controlled study. Neurology 80 (15), 1400–1405. https://doi.org/10.1212/wnl.0b013e31828c2f66.
Spiegler, A., Hansen, E.C.A., Bernard, C., McIntosh, A.R., Jirsa, V.K., 2016. Selective activation of resting-state networks following focal stimulation in a connectome-based network model of the human brain. eNeuro 3 (5). https://doi.org/10.1523/ENEURO.0068-16.2016.
Spiegler, A., Abadchi, J.K., Mohajerani, M., Jirsa, V.K., 2020. In silico exploration of mouse brain dynamics by focal stimulation reflects the organization of functional networks and sensory processing. Network Neurosci. 4 (3), 807–851. https://doi.org/10.1162/netn_a_00152.
Stefanovski, L., Triebkorn, P., Spiegler, A., Diaz-Cortes, M.-A., Solodkin, A., Jirsa, V., McIntosh, A.R., Ritter, P., Alzheimer's Disease Neuroimaging Initiative, 2019. Linking molecular pathways and large-scale computational modeling to assess candidate disease mechanisms and pharmacodynamics in Alzheimer's Disease. Front. Comput. Neurosci. 13, 54. https://doi.org/10.3389/fncom.2019.00054.
Stefurak, T., Mikulis, D., Mayberg, H., Lang, A.E., Hevenor, S., Pahapill, P., Saint-Cyr, J., Lozano, A., 2003. Deep brain stimulation for Parkinson's disease dissociates mood and motor circuits: a functional MRI case study. Mov. Disord. 18 (12), 1508–1516. https://doi.org/10.1002/mds.10593.
Terman, D., Rubin, J.E., Yew, A.C., Wilson, C.J., 2002. Activity patterns in a model for the subthalamopallidal network of the basal ganglia. J. Neurosci. 22 (7), 2963–2976. https://doi.org/10.1523/jneurosci.22-07-02963.2002.
Thomas, C., Ye, F.Q., Irfanoglu, M.O., Modi, P., Saleem, K.S., Leopold, D.A., Pierpaoli, C., 2014. Anatomical accuracy of brain connections derived from diffusion MRI tractography is inherently limited. Proc. Natl. Acad. Sci. 111 (46), 16574–16579. https://doi.org/10.1073/pnas.1405672111.
Triebkorn, P., Stefanovski, L., Dhindsa, K., Diaz-Cortes, M.-A., Bey, P., Bülau, K., Pai, R., Spiegler, A., Solodkin, A., Jirsa, V., McIntosh, A.R., Ritter, P., for the Alzheimer's Disease Neuroimaging Initiative, 2021. Brain simulation augments machine-learning–based classification of dementia. *Alzheimer's & Dementia: translational research & clinical interventions*. https://doi.org/10.1002/trc2.12303.
Tzourio-Mazoyer, N., Landeau, B., Papathanassiou, D., Crivello, F., Etard, O., Delcroix, N., Mazoyer, B., Joliot, M., 2002. Automated anatomical labeling of activations in SPM using a macroscopic anatomical parcellation of the MNI MRI single-subject brain. NeuroImage 15 (1), 273–289. https://doi.org/10.1101/2021.02.27.433161.
van Hartevelt, T.J., Cabral, J., Deco, G., Møller, A., Green, A.L., Aziz, T.Z., Kringelbach, M.L., 2014. Neural plasticity in human brain connectivity: the effects of long term deep brain stimulation of the subthalamic nucleus in Parkinson's disease. PLoS One 9 (1), e86496. https://doi.org/10.1006/nimg.2001.0978.
Velliste, M., Kennedy, S.D., Schwartz, A.B., Whitford, A.S., Sohn, J.-W., McMorland, A.J. C., 2014. Motor cortical correlates of arm resting in the context of a reaching task and implications for prosthetic control. J. Neurosci. 34 (17), 6011–6022. https://doi.org/10.1523/JNEUROSCI.3520-13.2014.
Villagrasa, F., Baladron, J., Vitay, J., Schroll, H., Antzoulatos, E.G., Miller, E.K., Hamker, F.H., 2018. On the role of cortex-basal ganglia interactions for category learning: a neurocomputational approach. J. Neurosci. 38 (44), 9551–9562. https://doi.org/10.1523/JNEUROSCI.0874-18.2018.
Visser, S., Van Gils, S.A., 2014. Lumping Izhikevich neurons. EPJ Nonlinear Biomed. Phys. 2 (1), 1–17. https://doi.org/10.1140/epjnbp19.
Vitay, J., Dinkelbach, H.Ü., Hamker, F.H., 2015. ANNarchy: a code generation approach to neural simulations on parallel hardware. Front. Neuroinforma. 9, 19. https://doi.org/10.3389/fninf.2015.00019.
Vitek, J.L., Jain, R., Chen, L., Tröster, A.I., Schrock, L.E., House, P.A., Giroux, M.L., Hebb, A.O., Farris, S.M., Whiting, D.M., Leichliter, T.A., Ostrem, J.L., San Luciano, M., Galifianakis, N., Verhagen Metman, L., Sani, S., Karl, J.A., Siddiqui, M. S., Tatter, S.B., Starr, P.A., 2020. Subthalamic nucleus deep brain stimulation with a multiple independent constant current-controlled device in Parkinson's disease (INTREPID): a multicentre, double-blind, randomised, sham-controlled study. Lancet Neurol. 19 (6), 491–501. https://doi.org/10.1016/S1474-4422(20)30108-3.
Whitmer, D., de Solages, C., Hill, B., Yu, H., Henderson, J.M., Bronte-Stewart, H., 2012. High frequency deep brain stimulation attenuates subthalamic and cortical rhythms in Parkinson's disease. Front. Hum. Neurosci. 6, 155. https://doi.org/10.3389/fnhum.2012.00155.
Wingeier, B., Tcheng, T., Koop, M.M., Hill, B.C., Heit, G., Bronte-Stewart, H.M., 2006. Intra-operative STN DBS attenuates the prominent beta rhythm in the STN in Parkinson's disease. Exp. Neurol. 197 (1), 244–251. https://doi.org/10.1016/j.expneurol.2005.09.016.
Wong, K.-F., Wang, X.-J., 2006. A recurrent network mechanism of time integration in perceptual decisions. J. Neurosci. 26 (4), 1314–1328. https://doi.org/10.1523/JNEUROSCI.3733-05.2006.
Yu, Y., Wang, X., Wang, Q., Wang, Q., 2020. A review of computational modeling and deep brain stimulation: applications to Parkinson's disease. Appl. Math. Mech. 1–22. https://doi.org/10.1007/s10483-020-2689-9. English Edition.

Supplementary Material

of the article

Virtual deep brain stimulation: Multiscale co-simulation of a spiking basal ganglia model and a whole-brain mean-field model with The Virtual Brain

Jil M. Meier[1,2,*], Dionysios Perdikis[1,2], André Blickensdörfer[1,2], Leon Stefanovski[1,2], Qin Liu[1,2], Oliver Maith[3], Helge Ü. Dinkelbach[3], Javier Baladron[3], Fred H. Hamker[3] and Petra Ritter[1,2,*]

1) Berlin Institute of Health at Charité – Universitätsmedizin Berlin, Berlin, Germany
2) Charité – Universitätsmedizin Berlin, corporate member of Freie Universität Berlin and Humboldt-Universität zu Berlin, Department of Neurology with Experimental Neurology, Brain Simulation Section, Berlin, Germany
3) Department of Computer Science, Chemnitz University of Technology, Chemnitz, Germany

* corresponding authors: jil-mona.meier@charite.de and petra.ritter@charite.de; postal address: Charité - Universitätsmedizin Berlin, Charité Campus Mitte (CCM), Brain Simulation Section, Robert-Koch-Platz 4, 10115 Berlin, Germany

Details of the spiking network model

For an overview of all variables used in this study, we refer to Supplementary Table 1. For every neuron in a region node modeled as a spiking network, the membrane potential *V* was assumed to follow the equation

$$\begin{aligned}\dot{V} = n_2V^2 + n_1V + n_0 - U/C - g_{AMPA}(V - E_{AMPA}) \\ -g_{GABA}(V_m - E_{GABA}) + I_e + I_{DBS}\end{aligned} \tag{1}$$

$$\dot{U} = a(bV - U), \tag{2}$$

where a, b, n_0, n_1 and n_2 are region-specific parameters that were taken from literature as in (Maith et al., 2021) (Supplementary Table 2). Specifically, parameters for GPe, GPi, STN were taken from (Thibeault & Srinivasa, 2013), for striatum from (Humphries et al., 2009) and for thalamus taken from the phasic bursting model of (Izhikevich, 2004). If the membrane potential exceeds a certain threshold value V_{th}, i.e., $V > V_{th}$, a spike is emitted, V is set to a value c and U is incremented by a fixed amount d. The conductance follows the equation

$$\dot{g_s} = -g_s/\tau_s + \left[\sum_k \delta(t - t_k)\right]_s, \tag{3}$$

where $s \in \{AMPA, GABA\}$ and δ is the Kronecker delta. The last term of this previous equation is the increase of the conductance by a fixed amount after each incoming spike k at spike time t_k. The equations were taken from (Baladron et al., 2019), only I_{DBS} was added.

Similar to previous publications (Baladron et al., 2019; Maith et al., 2021), we simulated the above model in ANNarchy (Vitay et al., 2015) and applied the Euler method to solve the differential equations (Equations (1)-(3)) with a time step of $0.05ms$.

Supplementary Table 1: Glossary table of all the used variables of our multiscale model. *We list all used variables with a short description, possibly their assigned values and respective unit.*

variable	assigned value	unit	description
t	-	ms	time
dt	0.1	ms	TVB integration time step
Spiking network			
V	-	mV	membrane potential
U	-	$\frac{mV}{ms}$	recovery variable
C	region-specific, Table 1	$\frac{1}{pF}$	membrane capacity
I_e	region-specific, Table 1	pA	region-specific external current
I_{DBS}	GPi stimulus: -10 monophasic STN: -280 biphasic STN: 160	pA	DBS current
a	region-specific, Table 1	-	rate of recovery of U
b	region-specific, Table 1	-	sensitivity of recovery to subthreshold fluctuations of membrane potential
c	region-specific, Table 1	mV	after-spike reset value of V
d	region-specific, Table 1	$\frac{mV}{ms}$	after-spike increment of U
n_0	region-specific, Table 1	-	neuron-type specific parameter
n_1	region-specific, Table 1	-	neuron-type specific parameter
n_2	region-specific, Table 1	-	neuron-type specific parameter
V_{th}	striatum: 40 all others: 30	mV	spike threshold membrane potential
g_{AMPA}	-	nS	AMPA synaptic conductance
g_{GABA}	-	nS	GABA synaptic conductance

E_{AMPA}	0	mV	AMPA reversal potential
E_{GABA}	-90	mV	GABA reversal potential
τ_{AMPA}	10	ms	AMPA synapse time constant
τ_{GABA}	10	ms	GABA synapse time constant
Mean-field model			
$S_{n'}$	-	-	proportion of open synaptic ion channels
$R_{n'}$	-	$1/s$	instantaneous spike rate
τ_{syn}	1000	ms	synaptic time scale
γ	0.641	s	excitatory kinetic parameter
α	2710	nC^{-1}	excitatory sigmoidal function parameter
β	108	Hz	excitatory sigmoidal function parameter
θ	0.154	s	excitatory sigmoidal function parameter
$I_{syn_{n'}}$	-	nA	presynaptic current
I_o	0.3	nA	overall effective external input current
w_+	0.9	-	local excitatory recurrence
J_N	0.2609	nA	excitatory synaptic coupling
a_c	$1/256$	-	linear coupling parameter
b_c	0	-	linear coupling parameter
G	$15/C_{norm}$	-	global coupling constant
$C_{m'n'}$	-	-	connection weight from node n' to node m'
$\tau_{m'n'}$	-	ms	delay from node n' to node m'
Interface and connectivity			
$w_{n'n}$	-	-	interface weight / spike weight from proxy node n' to spiking node n
$\tau_{n'n}$	-	ms	spike delay from proxy node n' to spiking node n
t_{jk}	-	ms	spike time of neuron j

$N_{neurons}$	-	-	number of neurons in a population
N_{spikes}	-	-	number of spikes
R_{in_n}	-	$\frac{1}{ms}$	input rate
R_{int_n}	-	$\frac{1}{ms}$	integrated input rate
τ_{int}	100	ms	integration time constant
C_{norm}	control: $C_{norm} = 0.00068199$ patient: $C_{norm} = 0.000705308$	-	connectivity weight ratio
$w_{norm_{iSN}}$	control: 0.0382668 patient: 0.0380754	-	interface factor for iSN
$w_{norm_{dSN}}$	control: 0.0321123 patient: 0.0338178	-	interface factor for dSN
$w_{norm_{STN}}$	control: 0.311472 patient: 0.2894958	-	interface factor for STN
DBS stimulus			
a_{DBS}	monophasic: -35 biphasic: 20	V	stimulus amplitude
κ	8	pS	scaling factor
f	monophasic: 120 biphasic: 130	Hz	stimulus frequency
δ_{DBS}	0.3	ms	pulse width (of the first, short and high-amplitude phase for the biphasic stimulus)

STN: subthalamic nucleus; dSN: striatum, direct striatal spiny projection neurons; iSN: striatum, indirect striatal spiny projection neurons; DBS: deep brain stimulation.

Supplementary Table 2: Spiking network parameters. *Set parameter values for each of the neuronal populations modeled as a spiking network (values taken from (Maith et al., 2021)).*

Population	a	b	c (mV)	d	C	I_e	n_0	n_1	n_2
Striatum	0.05	−20	−55	377	50	0	61.65	2.59	0.02
GPi	0.005	0.585	-65	4	1	30	140	5	0.04
GPe	0.005	0.585	-65	4	1	12	140	5	0.04
STN	0.005	0.265	-65	2	1	3	140	5	0.04
Thalamus	0.02	0.25	-65	0.05	1	3.5	140	5	0.04

CxExcit	0.02	0.2	-72	6	1	50	140	5	0.04
CxInh	0.02	0.2	-72	6	1	0	140	5	0.04

CxExcit: excitatory population of the cortex; CxInh: inhibitory population of the cortex; GPi: internal globus pallidus; GPe: external globus pallidus; STN: subthalamic nucleus.

Details of the underlying connectivity

The generation of the atlas from Petersen and colleagues (2019) started from co-registering histological data (Gallay et al., 2008; Morel, 2007) and normative MRI-based CIT-168 atlas (Pauli et al., 2018) from the Human Connectome Project (Van Essen et al., 2013). As the used histological atlas is focused on the thalamus and BG, additional tracts were approximated by information from non-human studies. The resulting streamlines were manually curated by the neuroanatomists in a holographic augmented-reality interface to correct their three-dimensional approximation interactively and further validated with the underlying histological data. As a result, the connectome by Petersen et al. provides a precise three-dimensional representation of fiber tracts in the human brain and can be used with any existing parcellation to calculate structural connectivity, similar to the calculation from DTI.

Details about ANNarchy

Based on the code written by the user, ANNarchy automatically generates optimized C++ code, which can be run on different types of parallel hardware (e.g., on a multi-core system or graphical processing unit). Together with the simulation in automatically generated C++ code and the use of parallel computing, ANNarchy possesses a unique combination of properties, enabling detailed simulations at low computational costs. ANNarchy runs on GNU/Linux and OSX and is open source with freely available documentation and source code at http://annarchy.readthedocs.org and http://bitbucket.org/annarchy/annarchy. An overview of the functions and objects of ANNarchy that were integrated in the TVB-ANNarchy simulation framework is shown in Supplementary Figure 1.

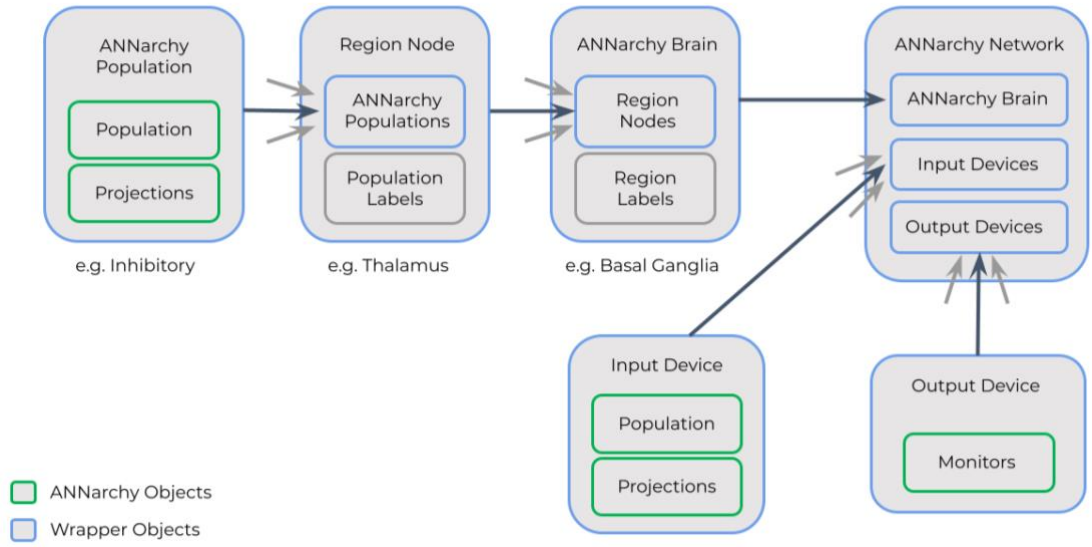

Supplementary Figure 1: Architecture of the TVB-ANNarchy co-simulation interface. *The different existing objects in ANNarchy are represented by gray boxes. The smallest defined objects*

are called devices and populations. A device ("ANNarchy Device") can be either an input or output device. Input devices contain special ANNarchy populations that can generate stimuli which can be used as inputs to other spiking populations. Output devices wrap around one or several ANNarchy monitors for recording spikes and state variables. A population object called "ANNarchy Population" wraps around a Population or Population View object from ANNarchy and also manages the projections between populations. In our use case, an ANNarchy Population can be an inhibitory population for example. A Region Node is one level above that in the hierarchy. It can contain several ANNarchy Populations and holds their labels. In our case, the thalamus is represented as a Region Node with one population. The ANNarchy Brain is on the next organisational level. It holds all Region Nodes and a mapping to their labels. The ANNarchy Network is the highest-level object. It holds an ANNarchy Brain as well as all Input Device and Output Device objects.Objects that exist in the ANNarchy library are colored in green, in blue are wrappers around them. Gray arrows indicate that several objects of the same type are typically held inside an object higher in the hierarchy, e.g., a Region Node can contain many ANNarchy Populations.

Supplementary Table 3: Firing rate validation between the ANNarchy model implementation by (Maith et al., 2021) and our TVB-ANNarchy implementation of the spiking-cortex model. *We compared the two spiking network implementations. For this validation, we performed a shorter simulation without noise on the control and patient network data.*

mean firing rate	ANNarchy model from (Maith et al., 2021) - control	spiking-cortex model inside TVB-ANNarchy - control	ANNarchy model from (Maith et al., 2021) - patient	spiking-cortex model inside TVB-ANNarchy - patient
Cx-E	16.0	16.0	16.0	16.0
Cx-I	32.0	32.0	32.0	32.0
dSN	16.4	16.6	19.2	18.9
iSN	15.8	15.8	15.4	15.9
STN	31.4	31.3	31.9	32.0
GPe	34.4	34.4	35.5	35.3
GPi	35.7	35.6	36.1	36.1
Thal	22.7	23.1	19.9	20.3

Cx-E: excitatory population of the cortex node; Cx-I: inhibitory population of the cortex node; GPi: internal globus pallidus; GPe: external globus pallidus; STN: subthalamic nucleus; dSN: striatum,

direct striatal spiny projection neurons; iSN: striatum, indirect striatal spiny projection neurons; Thal: thalamus.

Mean-field model for the cortical regions

For every region node $n\prime$ (we use the prime notation for nodes modeled only as mean-fields nodes in TVB), the (post-)synaptic gating dynamics $\dot{S_{n\prime}}$ (i.e., $S_{n\prime}$ is the proportion of synapse channels open at any given time) are defined as

$$\dot{S_{n\prime}} = -\frac{1}{\tau_{syn}} S_{n\prime}(t) + (1 - S_{n\prime}(t))\gamma R_{n\prime}(t),$$

where $\tau_{syn} = 1000ms$ is the time scale of the synapse and $R_{n\prime}(t)$ is the postsynaptic firing rate given by

$$R_{n\prime}(t) = \frac{\alpha I_{syn_{n\prime}}(t) - \beta}{1 - e^{-\theta(\alpha I_{syn_{n\prime}}(t) - \beta)}},$$

which is a sigmoidal activation function of the presynaptic input current $I_{syn_{n\prime}}$. The total presynaptic current is given by

$$I_{syn_{n\prime}}(t) = I_o + w_+ J_N S_{n\prime}(t) + a_c G J_N \sum_{m\prime \neq n\prime} C_{m\prime n\prime} S_{m\prime}(t - \tau_{m\prime n\prime}).$$

The variables $C_{m\prime n\prime}$ and $\tau_{m\prime n\prime}$ define the weight and delay for the connection from region node $n\prime$ to region node $m\prime$, respectively, whereby the sum runs over all pairwise combinations. The connectivity weights were additionally scaled by the global coupling constant G and the parameter a_c of TVB's linear coupling function (of the form $a_c x + b_c$, in which we set the default parameters $b_c = 0$ and $a_c = 1/256$). The parameters were determined as in (Deco et al., 2013) (Supplementary Table 1).

Details of the spike train generation for the coupling from TVB to ANNarchy

For the correlated spike trains' generation, TVB "proxy" nodes are modeled in ANNarchy, as populations Poisson-like spiking neurons whose population rate *x* varies following a stochastic differential equation

$$\frac{dx}{dt} = \frac{\mu - x}{\tau} + \sigma \frac{\xi}{\sqrt{\tau}},$$

where ξ is a random variable. Thus, the population rate x randomly varies around μ over time, with an amplitude determined by σ and a speed determined by τ. To avoid that x becomes negative, the values of μ and σ are computed from a rectified Gaussian distribution, parameterized by the desired population rate R_n, the desired correlation strength *corr = 0.3*, and the time constant $\tau = 10ms$. In our case, the rate was determined by TVB input at each TVB time step and μ and σ were automatically recomputed by the ANNarchy class *HomogeneousCorrelatedSpikeTrains* (Brette, 2009). The correlation parameter of the *HomogeneousCorrelatedSpikeTrains* ANNarchy spike generator was set to $corr = 0.3$ in all cases and models, after visual inspection and comparison of the generated spike trains to the spike trains of the noisy Izhikevich excitatory spiking cortex population

used in Maith et al. (2021), which was the driver of the spiking network in that study (Maith et al., 2021).

For the “trial and error” simulations for determining the value of G, we started with setting initial conditions of all $S_{n\prime} = 0.0$ and $R_{n\prime} = 0.0$. For every subsequent simulation, we were using the mean state variables’ values of the last 100 ms of the previous simulation as initial conditions. The mean firing rate that we were trying to approximate was also computed for those last 100 ms. Once the equilibrium was approximated and the mean firing rate was in the interval *[15, 18] Hz*, we set the G value accordingly and stored the initial conditions. For the *10* repetitive co-simulations for the results of Supplementary Table 4, we selected initial conditions randomly in the neighborhood of the above original vector of initial conditions as it is explained in the main text.

Small differences in the rates obtained for multiscale model’s co-simulations are to be expected, especially for the firing rate of the thalamus, which depends a lot on the spikes’ correlations among neurons of the populations that couple to it directly and indirectly. In that respect, please note that (a) the weighted superposition of the activity of many TVB “proxy” nodes results in an effective driving dynamics of a quite different autocorrelation profile than that of a single noisy spiking cortex node, and (b) we have set the same, undifferentiated, value for the correlation of the driving spike generators for both subjects, as explained above.

Details of the applied STN stimuli

The monophasic stimulus

$$I_{DBS} = a_{DBS} \cdot \kappa \cdot H\left(sin\left(2\pi f t\right)\right) \cdot \left(1 - H\left(sin\left(2\pi f(t + \delta_{DBS})\right)\right)\right)$$

is adapted from (Michmizos & Nikita, 2011), where H is the Heaviside function, f is the frequency in Hz, a_{DBS} is the amplitude of the stimulus in *V*, $\kappa = 8$ is a scaling factor, δ_{DBS} is the pulse width and t is the time in seconds. The biphasic stimulus was defined as

$$I_{DBS} = 1.1 \cdot a_{DBS} \cdot \kappa \cdot H\left(sin\left(2\pi \frac{f}{1000} t\right)\right) \cdot \left(1 - H\left(sin\left(2\pi \frac{f}{1000}(t - \delta_{DBS})\right)\right)\right)$$
$$-0.1 \cdot a_{DBS} \cdot \kappa \cdot H\left(sin\left(2\pi \frac{f}{1000} t\right)\right) \cdot \left(1 - H\left(sin\left(2\pi \frac{f}{1000}(t - (11 \cdot \delta_{DBS}))\right)\right)\right)$$

similar to (Liu et al., 2020). Here, the pulse width δ_{DBS} is the pulse width of the first, short and high-amplitude phase. The second phase of the biphasic stimulus is designed to be 10 times as long and has *1/10*th of the amplitude (Figure 6A). The parameters of the monophasic and the biphasic stimuli are listed in Supplementary Table 1.

Supplementary Table 4: Regions of the left hemisphere included in the connectome used for simulations. *The regions 1-5 are the regions of the basal ganglia network. The other regions are regions from the AAL atlas.*

Region number	Abbreviation of the region	Full region name
1	GPe	Globus pallidus externus

2	GPi	Globus pallidus internus
3	STN	Subthalamic nucleus
4	Striatum	Striatum
5	Thal	Thalamus
6	Precentral	Precentral gyrus
7	Frontal_Sup_2	Superior frontal gyrus
8	Frontal_Mid_2	Middle frontal gyrus
9	Frontal_Inf_Oper	Inferior frontal gyrus, opercular part
10	Frontal_Inf_Tri	Inferior frontal gyrus, triangular part
11	Frontal_Inf_Orb_2	Inferior frontal gyrus, orbital part
12	Rolandic_Oper	Rolandic operculum
13	Supp_Motor_Area	Supplementary motor area
14	Olfactory	Olfactory cortex
15	Frontal_Sup_Medial	Superior frontal gyrus, medial
16	Frontal_Med_Orb	Superior frontal gyrus, medial
17	Rectus	Gyrus rectus
18	OFCmed	Medial orbital gyrus
19	OFCant	Anterior orbital gyrus
20	OFCpost	Posterior orbital gyrus
21	OFClat	Lateral orbital gyrus
22	Insula	Insula

23	Cingulate_Ant	Anterior cingulate & paracingulate gyri
24	Cingulate_Mid	Middle cingulate & paracingulate gyri
25	Cingulate_Post	Posterior cingulate gyrus
26	Hippocampus	Hippocampus
27	ParaHippocampal	Parahippocampal gyrus
28	Amygdala	Amygdala
29	Calcarine	Calcarine fissure and surrounding cortex
30	Cuneus	Cuneus
31	Lingual	Lingual gyrus
32	Occipital_Sup	Superior occipital gyrus
33	Occipital_Mid	Middle occipital gyrus
34	Occipital_Inf	Inferior occipital gyrus
35	Fusiform	Fusiform gyrus
36	Postcentral	Postcentral gyrus
37	Parietal_Sup	Superior parietal gyrus
38	Parietal_Inf	Inferior parietal gyrus, excluding supramarginal and angular gyri
39	SupraMarginal	Supramarginal gyrus
40	Angular	Angular gyrus
41	Precuneus	Precuneus
42	Paracentral_Lobule	Paracentral lobule

43	Heschl	Heschl gyrus
44	Temporal_Sup	Superior temporal gyrus
45	Temporal_Pole_Sup	Temporal pole: superior temporal gyrus
46	Temporal_Mid	Middle temporal gyrus
47	Temporal_Pole_Mid	Temporal pole: middle temporal gyrus
48	Temporal_Inf	Inferior temporal gyrus
49	Cerebelum_Crus1	Crus I of cerebellar hemisphere
50	Cerebelum_Crus2	Crus II of cerebellar hemisphere
51	Cerebelum_3	Lobule III of cerebellar hemisphere
52	Cerebelum_4_5	Lobule IV, V of cerebellar hemisphere
53	Cerebelum_6	Lobule VI of cerebellar hemisphere
54	Cerebelum_7b	Lobule VIIB of cerebellar hemisphere
55	Cerebelum_8	Lobule VIII of cerebellar hemisphere
56	Cerebelum_9	Lobule IX of cerebellar hemisphere
57	Cerebelum_10	Lobule X of cerebellar hemisphere

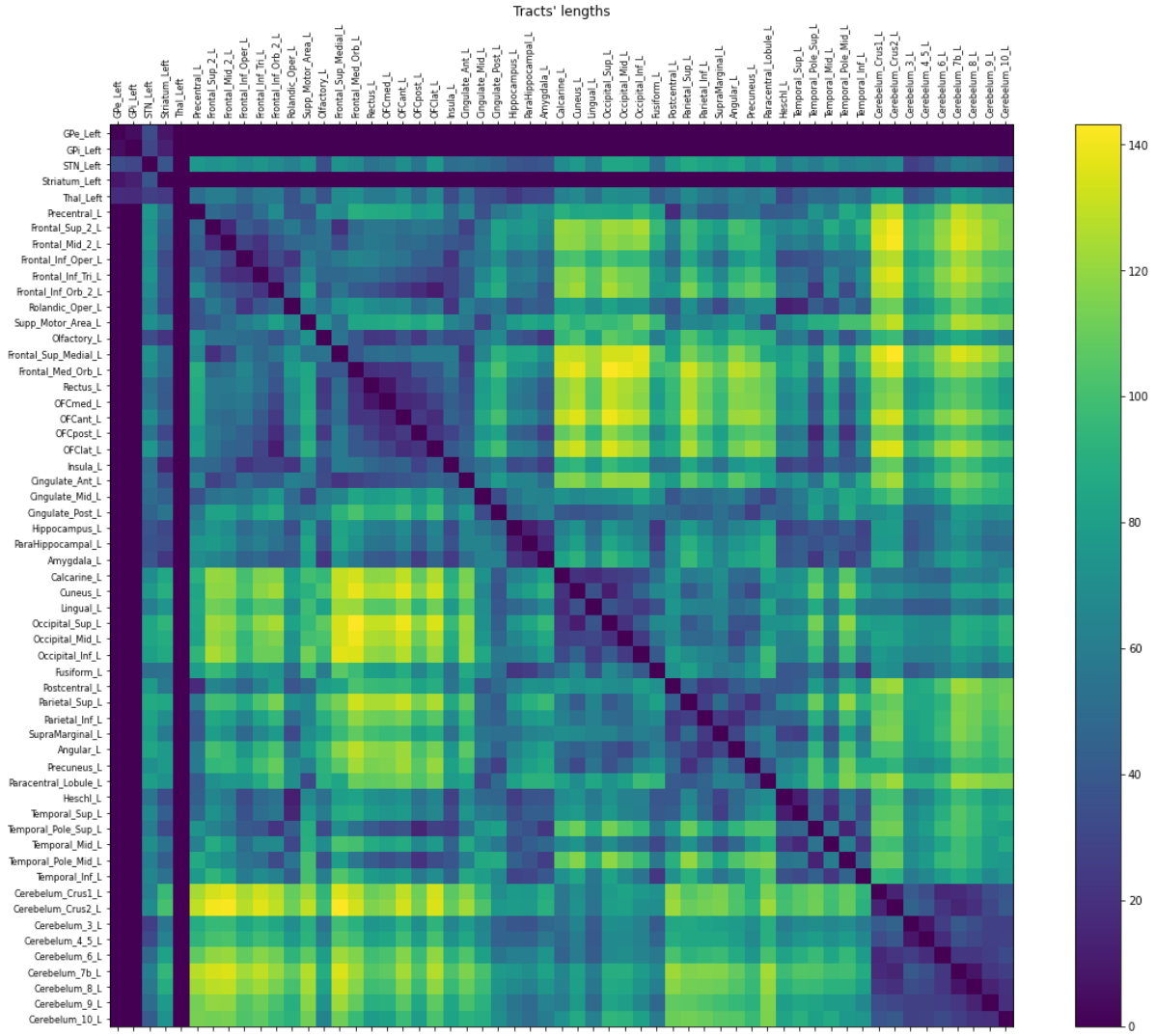

Supplementary Figure 2: Tract length matrix used for simulations. *We approximated the tract lengths among regions by the Euclidean distance between the three-dimensional anatomical center coordinates of each region.*

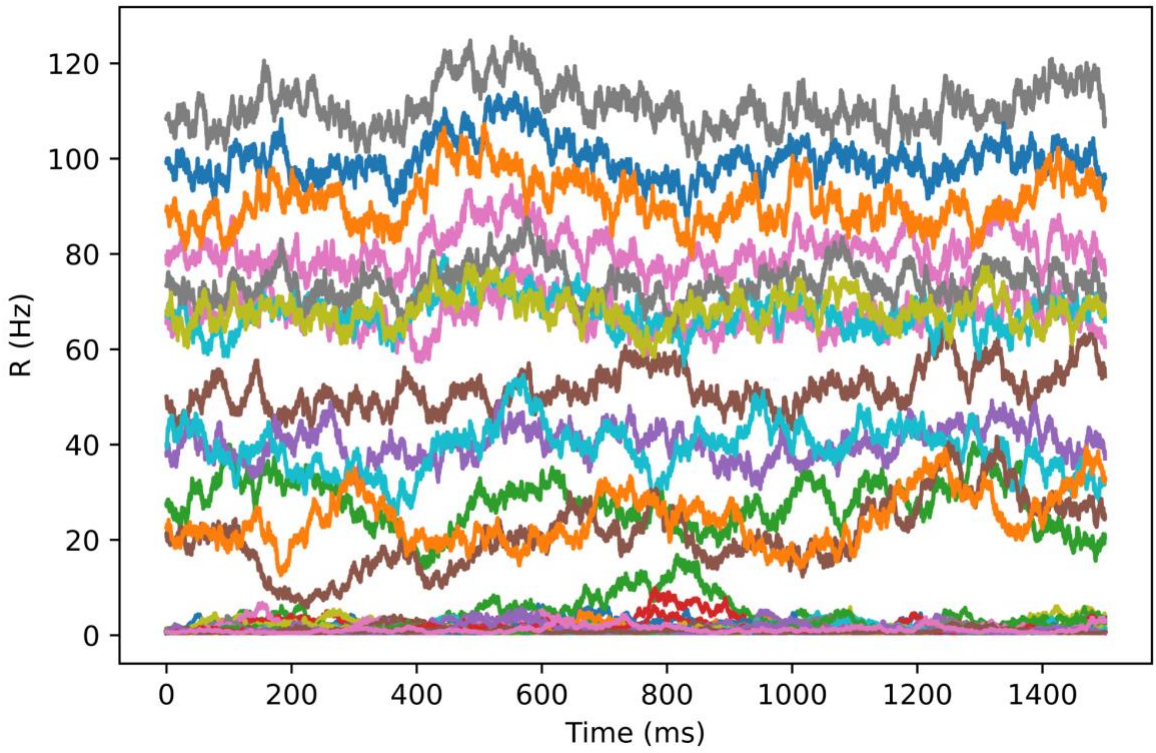

Supplementary Figure 3: Characteristic time series of the rate state variable R of all TVB nodes from a co-simulation. *Each colored time series represents the time series of the state variable R, the firing rate, of one of the TVB nodes. The dynamics consists of random fluctuations (due to additive white noise of standard deviation 10^{-4}) around an equilibrium point, which is determined by the couplings among the nodes on the basis of the structural connectome (weights and delays) and the global coupling scaling G. The mean firing rate across the whole TVB brain was on average 15 Hz. Despite not visually looking like it, this was the case because we had very low frequencies in multiple regions.*

Supplementary Table 5: Table of obtained firing rates for the spiking-cortex model for patient and control network, in both resting-state and stimulus condition. *Mean firing rates averaged over the last 1000ms of each simulation and averaged over the 10 repetition simulations in case of the TVB-cortex model (standard deviation of these mean firing rates over the 10 repetition simulations in case of the TVB-cortex model).*

mean firing rate	**resting-state control**		**resting-state patient**		**GPi-DBS patient**		**STN-DBS biphasic patient**		**STN-DBS monophasic patient**	
	spiking-cortex model	**TVB-cortex model**	**spiking-cortex model**	**TVB-cortex model**	**spiking-cortex model**	**TVB-cortex model**	**spiking-cortex model**	**TVB-cortex model**	**spiking-cortex model**	**TVB-cortex model**
Cx-E	14.1	-	14.1	-	14.1	-	14.1	-	14.1	-
dSN	16.2	16.2 (0.1)	19.9	20.7 (0.2)	22.8	23.4 (0.3)	22.8	22.3 (0.4)	21.5	22.7 (0.2)
iSN	10.8	10.3 (0.1)	9.5	8.9 (0.1)	11.4	11.0 (0.2)	10.9	10.3 (0.3)	10.5	10.6 (0.1)
STN	26.9	27.4 (0.1)	29.4	30.2 (0.1)	29.5	30.4 (0.1)	42.9	45.9 (0.2)	28.0	27.9 (0.2)
GPe	35.3	34.8 (0.3)	35.7	35.5 (0.1)	35.6	35.4 (0.2)	40.3	40.7 (0.5)	36.3	35.8 (0.2)
GPi	34.2	34.5 (0.1)	34.6	34.6 (0.1)	30.3	30.5 (0.1)	38.9	39.6 (0.3)	35.2	35.9 (0.1)
Thal	17.4	19.4 (0.2)	12.8	12.6 (0.3)	20.4	19.3 (0.5)	17.9	16.5 (0.9)	16.9	17.2 (0.3)

Cx-E: excitatory population of the cortex node; GPi: internal globus pallidus; GPe: external globus pallidus; STN: subthalamic nucleus; dSN: striatum, direct striatal spiny projection neurons; iSN: striatum, indirect striatal spiny projection neurons; Thal: thalamus.

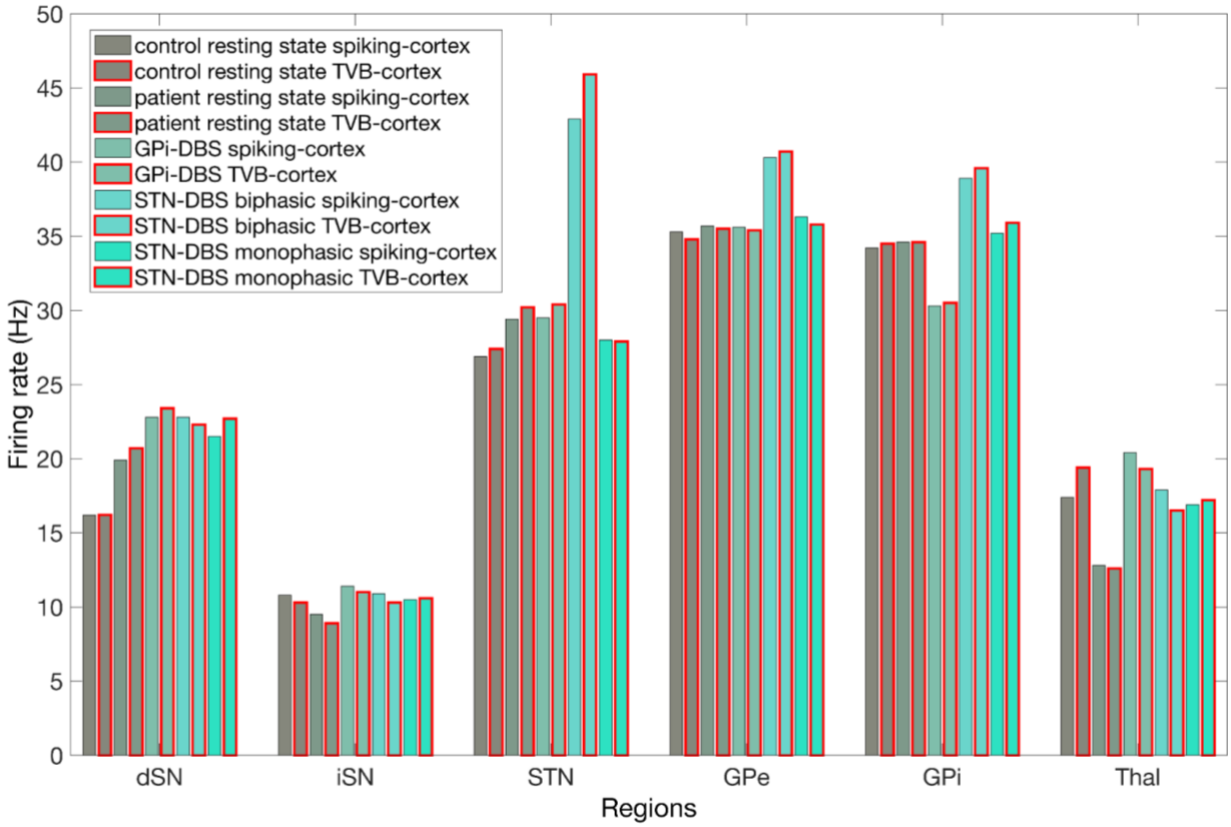

Supplementary Figure 4: Average firing rates obtained by different simulations of the TVB-cortex and the spiking-cortex model. *For each of the six spiking regions, each bar represents either the resting-state condition for the control, the patient or one of the three virtual DBS simulations, i.e., GPi-DBS, STN-DBS applying a biphasic and a monophasic stimulus. For each region, the first, third, fifth, seventh and ninth bars represent the average firing rate of the spiking-cortex model, the second, fourth, sixth, eighth and tenth bars (with red outline) represent the average firing rate of the TVB-cortex simulations. The heights of the bars represent the firing rate (in Hz) averaged over the last 1000 ms of the respective simulation and over the 10 simulation repetitions for the TVB-cortex simulations. GPi: internal globus pallidus; GPe: external globus pallidus; STN: subthalamic nucleus; dSN: striatum, direct striatal spiny projection neurons; iSN: striatum, indirect striatal spiny projection neurons; Thal: thalamus.*

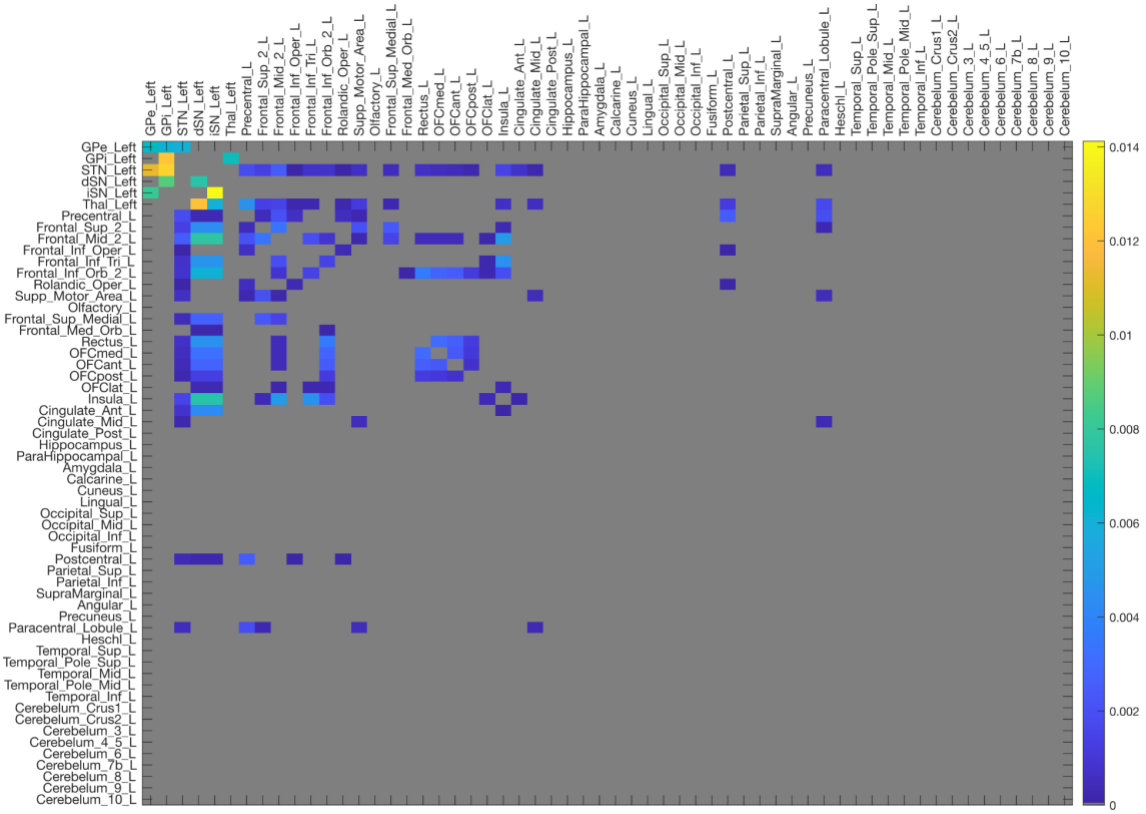

Supplementary Figure 5: Patient connectivity weight matrix used for multiscale simulations. *This connectivity matrix was used for the patient simulations. It does also include the disconnected nodes. Zero entries of the matrix are colored in gray. For visualization purposes, the normalized Petersen et al. (2019) connections have been brought to the same range as the optimally fitted connectivity weights from Maith et al. (2021).*

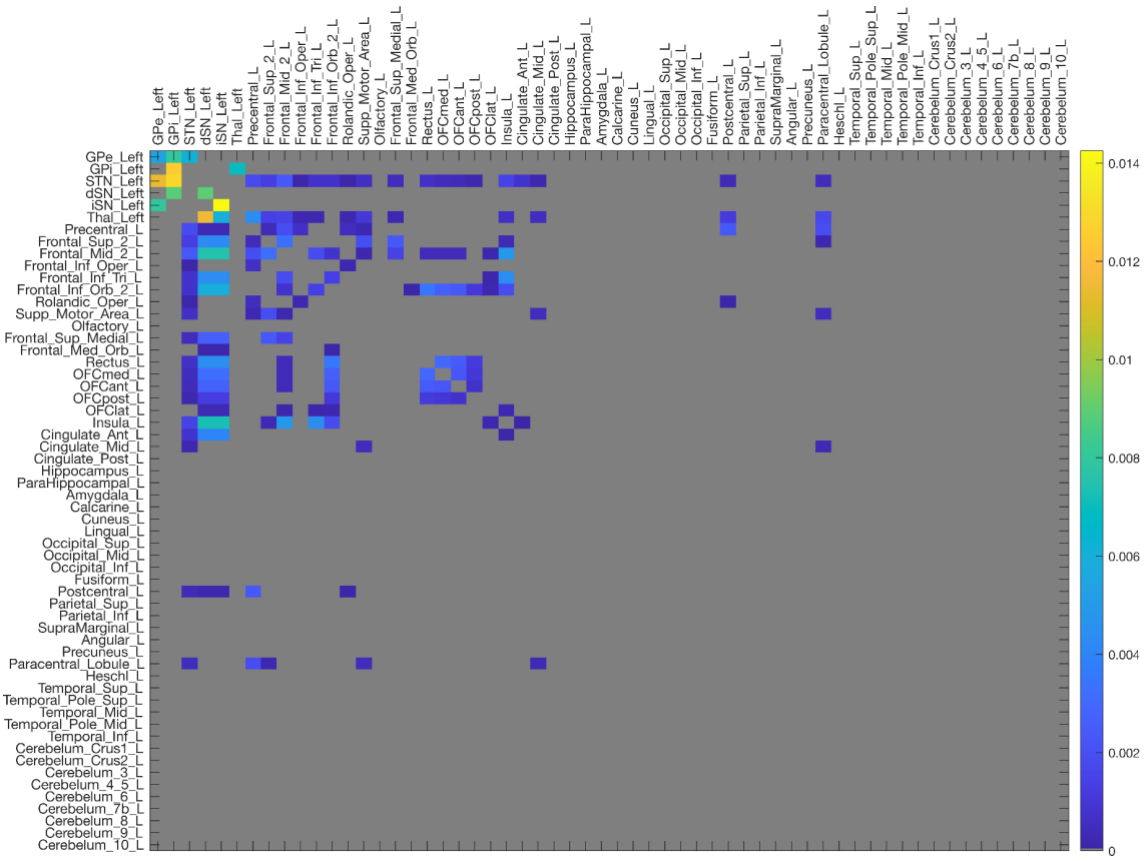

Supplementary Figure 6: Control connectivity weight matrix used for multiscale simulations. *This connectivity matrix was used for the control simulations. It does also include the disconnected nodes. Zero entries of the matrix are colored in gray. For visualization purposes, the normalized Petersen et al. (2019) connections have been brought to the same range as the optimally fitted connectivity weights from Maith et al. (2021).*

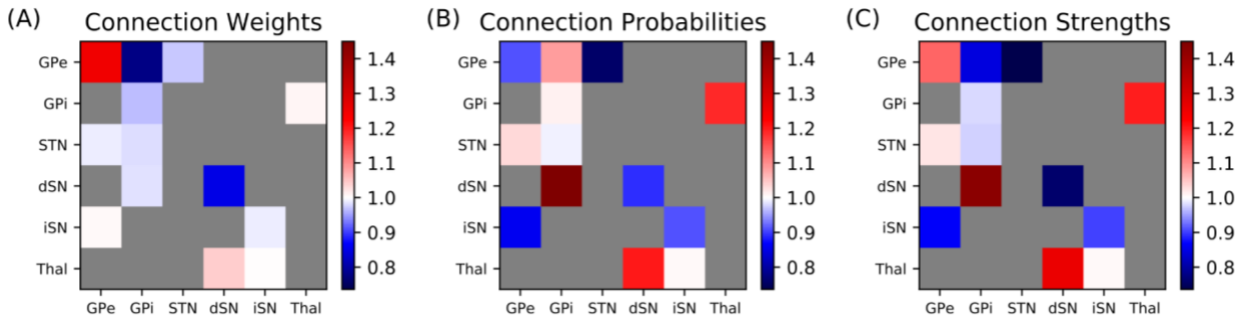

Supplementary Figure 7: Matrices visualizing the differences in connectivity weights, probabilities and strengths between patient and control BG spiking networks. *We obtained these matrices by dividing the parameter of the patient in the BG spiking network by the control parameter. Thus, an entry of 0.95 means that the patient has 95% of the control parameter value. Gray entries represent that there exists no connection between the pair of regions in our model. The analyzed parameters are (A) connection weights, (B) connection probabilities and (C) connection strengths. The connection strength is the product of the connection weight and probability similar as in Maith et al. (2021).*

References

Baladron, J., Nambu, A., & Hamker, F. H. (2019). The subthalamic nucleus-external globus pallidus loop biases exploratory decisions towards known alternatives: a neuro-computational study. *The European Journal of Neuroscience*, *49*(6), 754–767.

Brette, R. (2009). Generation of correlated spike trains. *Neural Computation*, *21*(1), 188–215.

Deco, G., Ponce-Alvarez, A., Mantini, D., Romani, G. L., Hagmann, P., & Corbetta, M. (2013). Resting-State Functional Connectivity Emerges from Structurally and Dynamically Shaped Slow Linear Fluctuations. *The Journal of Neuroscience: The Official Journal of the Society for Neuroscience*, *33*(27), 11239–11252.

Gallay, M. N., Jeanmonod, D., Liu, J., & Morel, A. (2008). Human pallidothalamic and cerebellothalamic tracts: anatomical basis for functional stereotactic neurosurgery. *Brain Structure & Function*, *212*(6), 443–463.

Humphries, M. D., Wood, R., & Gurney, K. (2009). Dopamine-modulated dynamic cell assemblies generated by the GABAergic striatal microcircuit. *Neural Networks: The Official Journal of the International Neural Network Society*, *22*(8), 1174–1188.

Izhikevich, E. M. (2004). Which model to use for cortical spiking neurons? *IEEE Transactions on Neural Networks / a Publication of the IEEE Neural Networks Council*, *15*(5), 1063–1070.

Liu, C., Zhao, G., Wang, J., Wu, H., Li, H., Fietkiewicz, C., & Loparo, K. A. (2020). Neural network-based closed-loop deep brain stimulation for modulation of pathological oscillation in Parkinson's disease. *IEEE Access*, 8, 161067–161079.

Maith, O., Villagrasa Escudero, F., Dinkelbach, H. Ü., Baladron, J., Horn, A., Irmen, F., Kühn, A. A., & Hamker, F. H. (2021). A computational model-based analysis of basal ganglia pathway changes in Parkinson's disease inferred from resting-state fMRI. *The European Journal of Neuroscience*, *53*(7), 2278–2295.

Michmizos, K. P., & Nikita, K. S. (2011). Addition of deep brain stimulation signal to a local field potential driven Izhikevich model masks the pathological firing pattern of an STN neuron. *Conference Proceedings: ... Annual International Conference of the IEEE Engineering in Medicine and Biology Society. IEEE Engineering in Medicine and Biology Society. Conference*, *2011*, 7290–7293.

Morel, A. (2007). *Stereotactic Atlas of the Human Thalamus and Basal Ganglia*. CRC Press.

Pauli, W. M., Nili, A. N., & Tyszka, J. M. (2018). A high-resolution probabilistic in vivo atlas of human subcortical brain nuclei. *Scientific Data*, 5, 180063.

Thibeault, C. M., & Srinivasa, N. (2013). Using a hybrid neuron in physiologically inspired models of the basal ganglia. *Frontiers in Computational Neuroscience*, 7, 88.

Van Essen, D. C., Smith, S. M., Barch, D. M., Behrens, T. E. J., Yacoub, E., Ugurbil, K., & WU-Minn HCP Consortium. (2013). The WU-Minn Human Connectome Project: an overview. *NeuroImage*, *80*, 62–79.

Vitay, J., Dinkelbach, H. Ü., & Hamker, F. H. (2015). ANNarchy: a code generation approach to neural simulations on parallel hardware. *Frontiers in Neuroinformatics*, 9, 19.